

## A cross-correction LiDAR SLAM method for high-accuracy 2D mapping of problematic scenario

Shoujun Jia, Chun Liu\*, Hangbin Wu, Doudou Zeng, Mengchi Ai

*College of Surveying and Geo-informatics, Tongji University, Shanghai 200092, PR China*



### ARTICLE INFO

**Keywords:**

High-accuracy 2D map  
Indoor modeling  
Cross-correction SLAM  
Mobile LiDAR  
Problematic scenario

### ABSTRACT

Highly accurate 2D maps can supply basic geospatial information for efficient and accurate indoor building modeling. However, problematic scenarios, which are characterized by few features, similar components and large scales, seriously influence data association and cumulative error elimination, and thus degrade simultaneous localization and mapping (SLAM)-based mapping quality. In this paper, a cross-correction LiDAR SLAM method is proposed for constructing high-accuracy 2D maps of problematic scenarios. The method comprises two models. The first model, namely, pose correction for rough mapping (PCRM), increases the data association capacity and generates a rough map with cumulative errors. In the PCRM model, a rough mapping module is developed against the scenario with few features for accurate data association. This module improves the robustness of the data association by using the initial poses from the local pose correction module, especially in similar-component scenarios. The other is a map correction for pose optimization (MCPO) model, which enhances cumulative error elimination capacity. Here, a block-based local map correction module is proposed that takes both map and pose into consideration to construct accurate constraints. The constraints are then added to the global pose optimization module to significantly reduce the cumulative error of the rough map and thus construct a high-accuracy 2D map. The results demonstrate the superiority of our method over 5 other state-of-the-art methods in problematic scenarios. The overall performance of our method in these two scenarios is approximately 1 cm and 0.2% in terms of the absolute and relative map errors, respectively. Moreover, the modeling results demonstrate that our method can be applied to the efficient and accurate indoor modeling.

### 1. Introduction

With the rapid development of geospatial information services, efficient and accurate indoor modeling has received much attention in a wide range of applications such as digital twin cities (Becker et al., 2015); building management (Boyes et al., 2017), energy simulations (Rafiee et al., 2014) and indoor navigation (Diaz-Vilarino et al., 2016). Recently, several important innovations have been made in 3D indoor modeling (Wang, 2018; Ochmann et al., 2016; Oesau et al., 2014; Ochmann et al., 2019), such as surface element-based (Ochmann et al., 2019) and semantic line framework-based methods (Wang, 2018). However, these modeling methods experience low computational efficiency, and may not be widely applied in practical situations (Cui and Dong, 2019). More importantly, considering that the performance of modeling significantly depends on the mapping quality, these methods may not accurately survey boundaries and sizes in scenarios due to the challenges of data collection and 3D mapping (Wang, 2018). Generally,

based on a high-accuracy 2D map, 3D model of scenario can be efficiently and accurately constructed (Cui and Dong, 2019), which is considered more applicable in practical situations than the existing 3D modeling methods. Therefore, a high-accuracy 2D map is crucial for efficient and accurate 3D indoor modeling.

Several methods have been developed for constructing 2D maps of scenarios, such as manual survey and simultaneous localization and mapping (SLAM)-based mobile mapping. In particular, SLAM-based method has been reported to efficiently survey boundaries and sizes in scenarios (Cadena, 2016; Bailey and Durrant-Whyte, 2006; Thrun, 2001). Moreover, among the sensors used for mobile mapping, such as scanning LiDAR sensors, cameras and color and depth (RGBD) sensors, the advantage of the single-line scanning LiDAR sensors is significant because of their high observation precision, low data processing cost and strong robustness to motion blur and illumination changes (Ren et al., 2019). Therefore, a single-line LiDAR mapping strategy is a more suitable choice for constructing 2D maps of scenarios in practical situations.

\* Corresponding author.

E-mail address: liuchun@tongji.edu.cn (C. Liu).

Generally, the quality of LiDAR SLAM-based mapping is determined by the front-end data association and back-end optimization performance (Grisetti et al., 2010.). However, some problematic environments may make data association and optimization difficult, and thus the accuracy and consistency of constructed map may be badly affected. In this paper, problematic environment refers to two different scenarios. One is a scenario with similar components and few features. There may be few distinctive features in LiDAR scans and no obvious changes between two consecutive scanning outputs, which seriously degrades the performance of data association (Wang et al., 2018; Wen et al., 2018). The other is defined as large-scale scenario. In large-scale and long-term mobile mapping process, the errors caused by data association are liable to accumulate over time, which poses great challenges for back-end optimization (Ren et al., 2019; Bosse and Zlot, 2008). Therefore, developing an accurate and robust LiDAR SLAM method to increase the capacities of data association and error elimination is highly advisable.

In this paper, a cross-correction SLAM method is proposed that can overcome problematic scenarios and construct high-accuracy 2D maps. The rest of this paper is organized as follows: The related work is briefly reviewed below, followed by the paper contributions. The details of the cross-correction LiDAR SLAM method are introduced in Section 2. Section 3 presents the experimental results and analysis. Section 4 describes the discussion. Finally, conclusions are given in Section 5.

### 1.1. Related work

This section briefly reviews LiDAR SLAM-based mapping methods. In general, the process of LiDAR SLAM consists of front-end and back-end stages. The front end, which includes sensor fusion and data association, outputs a rough map with cumulative error. The process of constructing the rough map is called rough mapping in this paper. In addition, the constructed map is optimized in the back-end stage to reduce the cumulative error.

#### 1.1.1. Sensor fusion

The sensor fusion approach can be used to reduce pose drift for accurate and robust data association. The method can usually be divided into two classes, namely, particle filter (PF) and extended Kalman filter (EKF). For example, a PF-based method represents a posterior probability based on a set of particles to estimate the pose state (Yatim and Buniyamin, 2015; Blanco et al., 2008). In particular, to reduce the uncertainty of the robot pose, Gmapping (Grisetti et al., 2007) a popular PF-based approach utilized both LiDAR observation and odometry information to calculate the particle distribution. Based on the PF framework, a six degree of freedom inertial measurement unit (6DOF IMU) and single-line LiDAR sensor were integrated (Baglietto et al., 2011) to reduce position drift for accurate human navigation. The advantage of PF-based sensor fusion approaches is that these methods can handle nonlinear, non-Gaussian distribution, and multimodal problems. However, the resampling phase can result in the loss of sample validity and diversity, which may degrade the sensor fusion performance (Yatim and Buniyamin, 2015). In addition, more particles and higher complexity are required for a larger-scale complex environment, which leads to higher computation cost. Thus, the PF-based method is not applicable to large-scale scenarios. The second type of sensor fusion approach, namely, EKF-based sensor fusion (D'Alfonso et al., 2015), is also a kind of probabilistic filter-based approach. The method recursively computes the conditional probability distribution of the state for pose estimation and mapping. Various improving forms of this approach have been developed in (Huang and Dissanayake, 2007; Zhang et al., 2017) for different environments. With the EKF framework, an IMU sensor was used in the Hector SLAM method (Kohlbrecher et al., 2011) to provide an initial pose estimation for addressing the least squares problems. In (Wang et al., 2018), an IMU-assisted 2D SLAM approach (LTDE) was proposed for low-texture and dynamic environments. An IMU-aided laser scan matching approach was achieved in

(Qian et al., 2019) for 2D indoor mapping. With these methods, the fusion of IMU and LiDAR sensors can estimate the initial pose to improve the robustness of the data association. Moreover, these methods can achieve better results when the sensor noise satisfies the Gaussian distribution and the measurement models are linear. More importantly, the EKF-based sensor fusion method is considered to have lower computational cost compared with those of the PF-based methods, especially for large-scale scenarios.

#### 1.1.2. Data association

Data association aims to match the currently observed scan with the previously scanned data and can be classified into three general matching forms, namely, feature-based scan matching, scan-to-scan matching and scan-to-map matching. The feature-matching algorithm extracts points and line segments as features from a scan and matches them with the features detected in a reference scan or given map (Choi et al., 2008; An et al., 2012). The method in (Jensfelt and Kristensen, 2001) extracts corner and step edge points, and constructs a complete feature graph for global scan matching. In (Gutmann et al., 2001), a line extraction and matching algorithm was proposed to detect line segments as features. An approach (Opronolla et al., 2017) for robust detection of line features from range data was developed based on the principal component analysis (PCA) algorithm. With these methods, feature-based scan matching is easy to understand and execute due to low complexity. However, for problematic scenarios with few features and similar components, there may be few features in a LiDAR scan and the scan may contain several similar but not corresponding features. These scenarios may cause scans to mismatch or even fail to match.

The scan-to-scan matching method directly utilizes two consecutive scans directly to compute their relative motion. For example, the classical algorithm is iterative closed point (Besl and McKay, 1992), which minimizes the total distance between the corresponding points contained in two scans for point-to-point matching. This method has been further improved such as polar scan matching (Diosi and Kleeman, 2005) and iterative closed line (Censi and Ieee, 2008) algorithms. These methods are used to calculate the rigid transformation between consecutive scanning frames. The normal distribution transform matching method was proposed in (Biber and Ieee, 2003) to associate a new scanning result and a reference scan that is based on a normal distribution to collectively describe a scan within each subdivided grid space. In these cases, the advantages of these approaches are considered to be their low computational complexity, as only two consecutive scans are computed in each matching process. However, featureless and similar-component scenario may pose great difficulty for scan-to-scan matching. In addition, due to incorrect scan matching, errors accumulate rapidly over time, especially in large-scale scenarios. Thus, problematic environments significantly degrade the performance of the scan-to-scan matching.

Alternatively, the scan-to-map matching is one of the most popular data association methods for LiDAR-based mobile mapping. The matching process directly associates the current observed scan with many existing scans or maps. Some methods, such as LSO (Ren et al., 2019), LTDE (Wang et al., 2018), CNC (Wen et al., 2018), Cartographer (Hess et al., 2016) and Hector SLAM (Kohlbrecher et al., 2011), achieved the scan-to-map matching strategies that align the current scanning set with the map. In (Wen et al., 2018; Bachrach et al., 2011.; Tang et al., 2014), maximum likelihood estimation methods were developed to improve the accuracy of scan matching, which were based on an occupancy likelihood map that contains useful structure and noise information collected by sensors. Using a probabilistic framework, a popular scan-to-map matching method, the correlative scan matcher (CSM), was developed in (Olson and Ieee, 2009) to search for the best rigid transformation between the current scan and the existing map. In (Chong et al., 2013; Olson and Ieee, 2015), the CSM approaches were improved for accurate and robust scan matching. In this case, due to the greater number of features contained in the local map, the scan-to-map

matching strategy can improve the scan matching performance in the scenarios with few features and limit the error accumulation in small-scale scenarios. Nevertheless, the performance of scan-to-map matching degrades in similar-component environments. Moreover, these methods have higher computational loads since the current scan needs to be associated with many scans rather than only one.

### 1.1.3. Back-end optimization

To eliminate the error accumulated in the data association process, the optimization methods have been applied in the back-end stage to improve the accuracy of mapping results. The graph-based map optimization is the most popular approach used for nonlinear optimization in mobile mapping (Grisetti et al., Win 2010.). In this method, a collection of edges and nodes in the graph represent the adjacent constraints of observations and poses, respectively, and then loop closing constraints are added to the optimization problem to reduce the pose drift for map optimization (Latif et al., 2013). In particular, the performance of the graph-based map optimization method is highly dependent on the accuracy of the loop closing constraints (Konolige et al., 2010). Various graph-based methods have already been achieved in previous works. For example, a reliable loop closing constraint was constructed in (Bosse and Zlot, 2008) based on the entropy sequences of projection histograms and an exhaustive correlation for outdoor environments. In (Himstedt et al., 2014), a feature-based constraint construction method was developed based on the fast laser interest point transform descriptor. A learning-based method (Li et al., 2017) was proposed for loop closure constraints in indoor environments. The approach of Cartographer (Hess et al., 2016) computed scan matches as loop closure constraints to reduce the computational requirements. In the LSO method (Ren et al., 2019), the AdaBoost algorithm was also introduced to build robust loop closure constraint. The methods described above can provide effective loop closure constraints for map optimization to complete different tasks. However, accurate and robust loop closure constraints are difficult to construct in similar and featureless environments. To address this problem, the CNC approach (Wen et al., 2018) added high-precision geometry taken by distance measurements as loop closure constraints, which can be insensitive to the problematic scenario. Nevertheless, this method is considered to be highly complex and dependent on prior knowledge, which limits its application.

For each LiDAR scan that consists of local map and its pose, there is a mutual-promotion mechanism between the pose and map. In detail, the correction of the initial pose can promote rough mapping, and then self-optimization of the rough map can facilitate pose optimization, further improving the accuracies of pose and map (Quan et al., 2019; Li et al., 2020). Unlike previous LiDAR SLAM studies on the front-end data association (Choi et al., 2008; An et al., 2012; Jensfelt and Kristensen, 2001; Gutmann et al., 2001; Opronolla et al., 2017; Besl and McKay, 1992; Dosi and Kleeman, 2005; Censi and Ieee, 2008; Biber and Ieee, 2003; Hess et al., 2016; Bachrach et al., 2011; Tang et al., 2014; Olson and Ieee, 2009; Chong et al., 2013; Olson and Ieee, 2015) and the back-end optimization (Latif et al., 2013; Konolige et al., 2010; Himstedt et al., 2014; Li et al., 2017), we explicitly take the mutual-promotion mechanism between the pose and map into account, so that the data association and error elimination can benefit from cross correction between the pose and map, thus improving the accuracy and robustness of LiDAR SLAM.

### 1.2. Contribution

In this paper, a cross-correction LiDAR SLAM method is proposed. The goal is to improve the accuracy and robustness of LiDAR SLAM for high-accuracy 2D mapping in problematic scenarios by increasing the data association and cumulative error elimination capacities. More specifically, given that the accuracy of data association is relatively high during short periods of time, a novel concept of “block” is proposed to quantitatively represent local maps. Based on the block, a rough

mapping module is developed to use more features for scan matching and limit error accumulation, which overcomes the scenarios with few features for accurate data association. Particularly, with the assistance of the initial poses provided by the sensor fusion results, this module can improve the robustness of data association, especially for similar-component scenarios. Moreover, a block-based local map correction module is proposed to construct accurate constraints for pose optimization. The constraints are from both the map and pose rather than only the traditional pose constraints obtained from scan matching, which are added into the global pose optimization to significantly improve the cumulative error elimination capacity. Thereby, the data association and cumulative error elimination capacities can be significantly improved and used to further increase the accuracy and robustness of LiDAR SLAM. The main contributions are summarized as follows:

- (1) A rough mapping module is proposed to overcome the scenarios with few features for accurate data association, and improve the robustness of data association in similar-component scenarios with the assistance of the initial pose from sensor fusion.
- (2) A local map correction module is devised to facilitate global pose optimization and thus significantly increase the cumulative error elimination capacity, especially for large-scale scenarios.
- (3) A cross-correction LiDAR SLAM method is constructed for high-accuracy mapping of problematic scenarios, by integrating the rough mapping module and the local map correction module into the traditional SLAM framework.
- (4) A comprehensive performance evaluation and analysis of the proposed methods and 5 other state-of-the-art methods on two different experimental datasets are presented.

## 2. The cross-correction LiDAR SLAM method

### 2.1. Overview

Using the mutual-promotion mechanism between pose and map, a cross-correction LiDAR SLAM method is proposed for constructing a high-accuracy 2D map of problematic scenarios. In the proposed method, the initial pose is corrected to promote rough mapping, and then the correction of the rough map can provide feedback for the global pose optimization. Hence, the process of cross-correction between the pose and map is completed. The flowchart of the proposed method, which contains two main models, is shown in Fig. 1.

**Model 1: Pose correction for rough mapping (PCRM).** This model is based on single-line LiDAR scans and low-cost IMU data. The local pose correction module outputs relatively accurate initial poses into the rough mapping module to reduce the uncertainty in the pose, especially for similar-component scenarios. In addition, the rough mapping module generates the rough map, in which a scan-to-block matching is proposed to improve the accuracy of the data association in the scenarios with few features.

**Model 2: Map correction for pose optimization (MCPO).** The map correction constraints are constructed in the block-based local map correction module to optimize local rough map. Then, the local map correction results are added as pose correction constraints to the global pose optimization module to further optimize the pose and map. The MCPO model facilitates improvement of the cumulative error elimination capacity, especially for large-scale scenarios, and outputs a high-accuracy 2D map.

### 2.2. Pose correction for rough mapping (PCRM)

The PCRM model increases the data association capacity against the scenarios with few features and similar components, and generates a rough map. For this purpose, the rough mapping module is proposed for accurate data association, which uses the initial pose estimated by the local pose correction module to improve the robustness of data

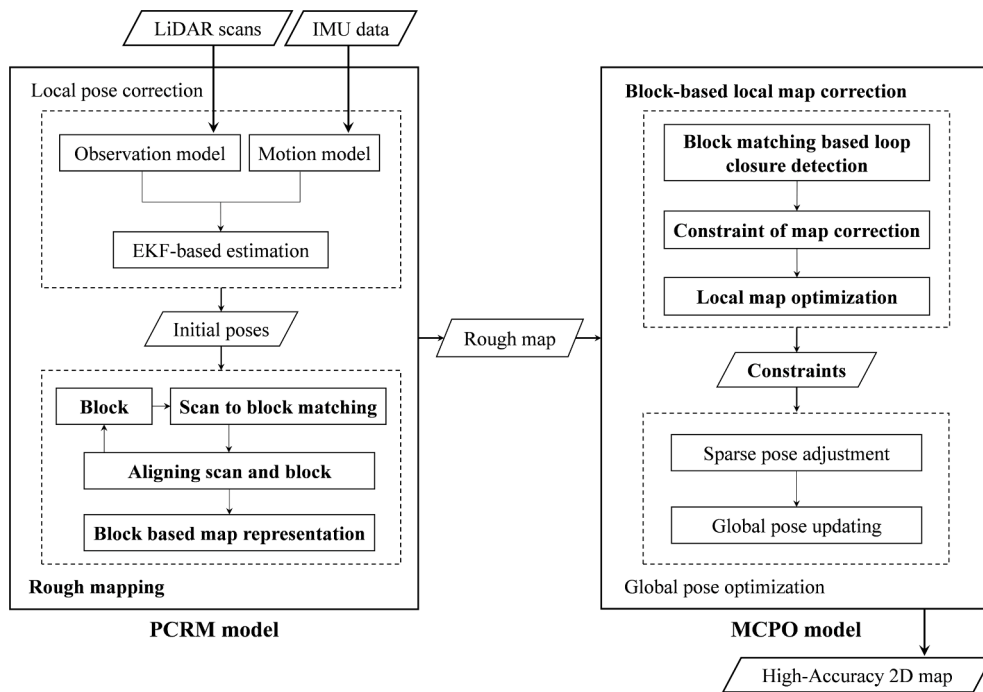


**Fig. 1.** Flowchart of the cross-correction LiDAR SLAM method, which contains two main models, namely, PCRM and MCPO.

association. This model contains two modules, namely, local pose correction and rough mapping.

### 2.2.1. Local pose correction

The local pose correction module is based on the EKF framework for estimating initial pose, which contains propagating and updating steps. The process is expressed in Fig. 2. The pose state vector of the mobile platform at time-step  $k$  can be described as  $X(k) = [q_{C_k}^W \ p_{C_k}^W \ v_{C_k}^W]^T$ , where  $q_{C_k}^W$  is the unit quaternion that denotes the rotation from frame  $\{C_k\}$  to  $\{W\}$ ,  $p_{C_k}^W = (x_k, y_k, z_k)^T$  represents the relative position of frame  $\{C_k\}$  in the  $\{W\}$  coordinate frame, and  $v_{C_k}^W \in \mathbb{R}^3$  is the velocity of frame  $\{C_k\}$  with respect to  $\{W\}$ .

The prediction model of the EKF-based sequential adjustment is provided by the IMU measurements, which can be expressed as  $u = [\omega \ Ta \ T]^T$ , where  $\omega \in \mathbb{R}^3$  and  $a \in \mathbb{R}^3$  are the angular velocity and acceleration of the mobile platform with respect to frame  $\{C\}$ , respectively (Quan et al., 2019). According to the continuous state propagation

model, the discrete IMU state propagation model can be derived by using expectation and integration operators. The prediction of the IMU at time-step  $k-1$  is expressed as (Quan et al., 2019):

$$\hat{X}_C(k|k-1) = f_k \left( \hat{X}_C(k-1) \right) \quad (1)$$

Then, the linearized error function of the discrete IMU state propagation model can be denoted as:

$$\begin{cases} \delta \hat{X}_C(k|k-1) = F_k \delta \hat{X}_C(k-1) + G_k \eta_C \\ F_k = \frac{\partial f}{\partial X} \Big|_{X(k)} \end{cases} \quad (2)$$

where  $\eta_C = [\eta_\omega^T \ \eta_a^T \ \eta_b^T]^T$  denotes the system noise. Thus, the covariance matrix  $P(k|k-1)$  is propagated as follows:

$$P_C(k|k-1) = F_k P_C(k-1) F_k^T + G_k Q G_k^T \quad (3)$$

where  $Q = [\sigma_\omega^2 \ \sigma_a^2 \ \sigma_b^2]$  represents the diagonal covariance matrix of the

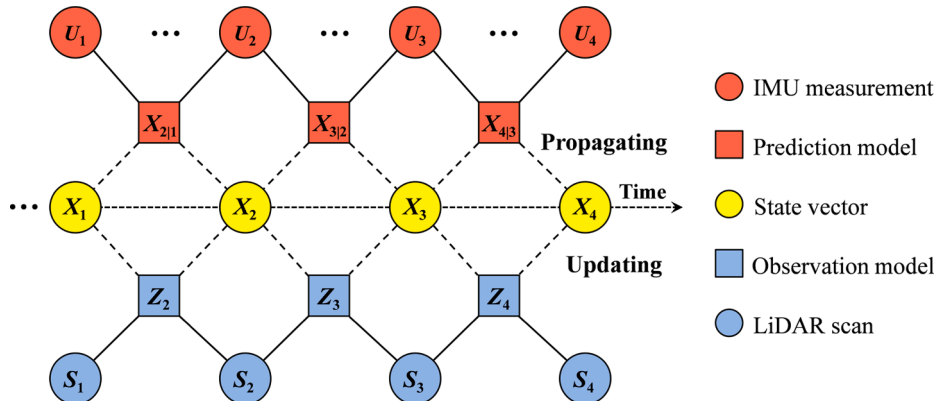


**Fig. 2.** A graphical illustration of EKF-based sequential adjustment indicating the processes of propagating and updating. Time increases along the horizontal direction from left to right, and the yellow circles represent the pose state of the mobile platform at each time step. (For interpretation of the references to color in this figure legend, the reader is referred to the web version of this article.)

noise.

Moreover, to eliminate the error caused by the IMU sensor, an observation model for the EKF-based sequential adjustment is constructed, which is based on the pose information of single-line LiDAR scans. Let,  $h_i \in R^2$  be the LiDAR points. The observation model can be expressed as:

$$Z_i = \begin{bmatrix} \rho_i \\ \theta_i \end{bmatrix} = h(X_i) + v_i \quad (4)$$

$$h(X_i) = \begin{bmatrix} \sqrt{(x_i - x)^2 + (y_i - y)^2} \\ \arctan\left(\frac{x_i - x}{y_i - y}\right) \end{bmatrix} \quad (5)$$

where  $\rho_i$  and  $\theta_i$  are the measurements of the LiDAR sensor, which denote the measured distance and polar angle of the LiDAR point  $h_i$  in the LiDAR coordinate frame  $\{S\}$ , respectively. In addition,  $(x_i, y_i)$  is the position of the LiDAR point  $h_i$ .  $(x, y)$  and  $\theta$  are location and orientation of the LiDAR sensor in the plane, respectively, and  $v_i$  represents the measurement error of the LiDAR sensor with covariance  $\Sigma_{v_i}$ . Subsequently, the linearized error function of the observation model can be derived as:

$$\begin{cases} \delta Z(k) = H_k \delta X(k) + v_k \\ H_k = \frac{\partial h}{\partial X} \Big|_{X(k)} \end{cases} \quad (6)$$

Then, the pose state vector and covariance matrix are updated as follows (D'Alfonso et al., 2015):

$$\begin{cases} K_k = P(k|k-1)H_k^T(H_kP(k|k-1)H_k^T + \Sigma_{v_k})^{-1} \\ \hat{X}(k|k) = \hat{X}(k|k-1) + K_k \delta Z(k) \\ P(k|k) = (I - K_k H_k)P(k|k-1) \end{cases} \quad (7)$$

where  $\Sigma_{v_k}$  denotes the covariance matrix of the LiDAR measurements and  $\hat{X}(k|k)$  and  $P(k|k)$  represent the updated pose state vector and covariance matrix, respectively.

### 2.2.2. Rough mapping

For LiDAR SLAM-based mobile mapping, the map is assumed to be a collection of LiDAR scans and their poses (Lu and Milius, 1997), as shown in Fig. 3. The LiDAR scan  $s = (H, \xi)$  refers to the LiDAR points as  $H = \{h_i\}_{i=1,\dots,I}$ ,  $h_i \in R^2$ , and the pose  $\xi$  consists of the location  $(x, y)$  and the orientation  $\theta$ . Let  $m$  be a map. The map at time-step  $t$  is expressed as:

$$m_t = \{(H_1, \xi_1), (H_2, \xi_2), \dots, (H_t, \xi_t)\}_{t=1,2,3,\dots} \quad (8)$$

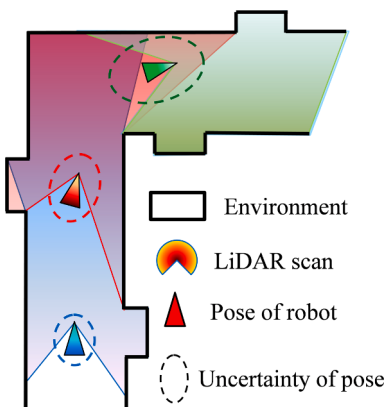


**Fig. 3.** A graphical illustration of LiDAR-based mobile mapping. The map is represented by scans and their respective poses. The alignment between the current scan and existing scans is used to localize the mobile platform.

where  $H_t$  represents a LiDAR scan at time-step  $t$  and  $\xi_t$  is its pose. The goal of mobile LiDAR mapping is to align a sequence of scans at the best estimated pose to construct the most likely map given the input data. This can be expressed as (Thrun et al., 2000):

$$\operatorname{argmin}_{m_t} \{1 - P(m_t|d_t)\} \quad (9)$$

where  $P(m_t|d_t)$  denotes the map likelihood and  $d_t$  is the input data, which contains LiDAR and IMU measurements in this paper.

Generally, to maximize the map likelihood (Eq. (9)), scan matching is used for estimating the global optimal poses of scans. Based on the probability grids, the LiDAR scan endpoints are rasterized to occupied positions, and the probabilities of the LiDAR observations are computed following the approach of a previous work (Thrun et al., 1998). The conditional probability  $P(z_i|\xi_t, m_{t-1})$  that the LiDAR sensor observes a scan point  $z_i$  given an environment map  $m_{t-1}$ , is computed for each perceptual point  $\{H_t\}$  in the scan (Thrun et al., 1998). The process of scan matching is repeated for each point in the map. The aim is to find the optimal scan pose to maximize the probabilities at the scan points. The process of scan matching can be expressed as a nonlinear least squares problem:

$$\operatorname{argmin}_{\xi_t} \sum_{i=1}^I (1 - P(z_i|\xi_t, m_{t-1}))^2 \quad (10)$$

$$\text{score} = \sum_{i=1}^I P(z_i|\xi_t, m_{t-1}) \quad (11)$$

where  $I$  is the number of LiDAR scan points,  $\xi_t$  denotes the initial pose of scan matching,  $\xi_t'$  is the optimal pose of the scan, and  $\text{score}$  represents the maximal probability of the optimal pose.

In practical situations, the performance of scan matching is seriously degraded in similar-component scenarios due to the increasing uncertainty in the mapping platform pose. As stated above, the robustness and accuracy of scan matching are highly dependent on the quality of the initial pose of scan matching (Wang et al., 2018; Baglietto et al., 2011). To address the problem of similar-component scenario, the local pose correction module is employed to estimate a relatively accurate pose. The estimated pose is used as the initial pose of scan matching (*i.e.*  $\xi_t$ ) to reduce the uncertainty of poses in similar-component scenarios. Thus, the local pose correction module participates in the process of scan matching and improves the rough mapping quality in problematic environments.

Moreover, the precision and cost of the probability computation increase with increasing grid resolution (Olson and Ieee, 2015). Because high-accuracy maps and large-scale scenarios are taken into account; the computation cost significantly increases. To reduce the computation cost, a triple-resolution probability grid is designed in our strategy, as shown in Fig. 4. Instead of computing the global optimum (*i.e.*,  $\text{score}$ ) at a constant resolution, our approach searches the  $\text{score}$  first in a rough-resolution grid with smaller parameter space. Then, on the middle-resolution grid,  $\text{score}$  is further searched only in the subspace at the optimum of the rough-resolution grid. Similarly, only the subspace at the optimum of the middle-resolution grid is further used, on the fine-resolution grid.

More importantly, since LiDAR scans encode little information in the scenarios with few features, it is difficult to detect enough distinctive features from scans for reliable and accurate scan matching, as shown in Fig. 5(a) and (b). Although both IMU integration and scan matching suffer from drift after a long period of accumulation, we consider that their accuracies are relatively high during short periods of time (Hess et al., 2016). Based on this assumption, a scan-to-block matching method is proposed in our strategy following the scan-to-map matching. Instead of an undefined submap with an uncertain range, our method defines the block as a collection of consecutive scans within a given

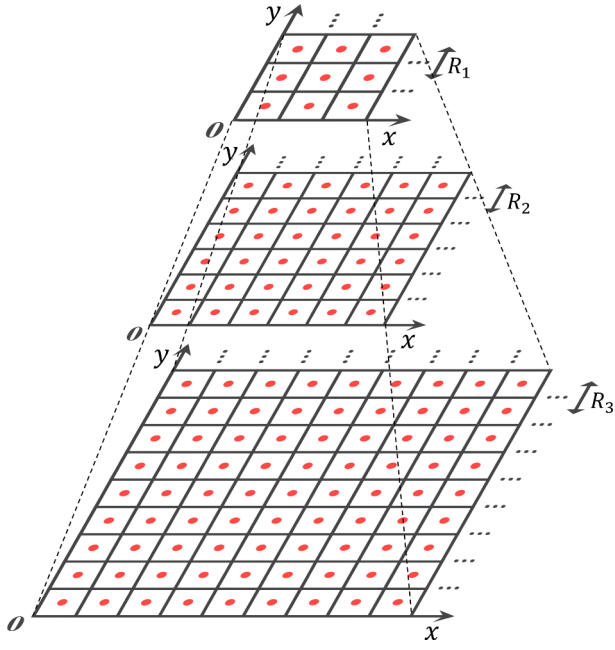


**Fig. 4.** Triple-resolution probability grids.  $R_1, R_2, R_3$  denote rough, middle and fine resolutions, respectively. The red circles represent the grid points, and the associated pixel of the grid point is defined as all points that are closest to that grid point. (For interpretation of the references to color in this figure legend, the reader is referred to the web version of this article.)

trajectory length of the mobile platform. In other words, when mobile platform moves more than a given length, the construction of a block is finished, as shown in Fig. 5(c). The block is described as follows:

$$B_l = \left\{ \left( s_1^l, s_2^l, s_3^l, \dots, s_j^l \right) \mid d \right\} \quad (12)$$

where  $B_l$  denotes the block,  $s_j^l$  is the LiDAR scan inserted in block (*i.e.*,  $B_l$ ) at the best estimated pose, and  $d$  is the trajectory length that the platform moves. Accordingly, the scan-to-block matching strategy is to

implement scan matching between a scan and a recent block, so more features can be used for data association in the scenarios with few features. As a block contains only a few dozen consecutive scans that are aligned at the best estimated poses, the scan-to-block matching accumulates error slowly and can achieve relatively high accuracy for a block. Based on the optimization problem of scan matching (Eq. (10)), scan-to-block matching can be expressed as:

$$\underset{\xi_t}{\operatorname{argmin}} \sum_{i=1}^I (1 - P(z_i | \mathcal{M}(\xi_t), B_{t-1}))^2 \quad (13)$$

$$\mathcal{M}(\xi_t) = \left\{ \xi_t \oplus (\Delta x \cdot R_x, \Delta y \cdot R_y, \Delta \theta \cdot R_\theta) \right\}_{(R_x, R_y, R_\theta) \in \overline{\mathcal{M}}} \quad (14)$$

$$\overline{\mathcal{M}} = \{-w_x, \dots, w_x\} \times \{-w_y, \dots, w_y\} \times \{-w_\theta, \dots, w_\theta\} \quad (15)$$

$$w_x = \text{INT}(W_x / \Delta x), w_y = \text{INT}(W_y / \Delta y), w_\theta = \text{INT}(W_\theta / \Delta \theta) \quad (16)$$

where  $B_{t-1}$  is the preceding block,  $(R_x, R_y, R_\theta)$  are the resolutions of the probability grid,  $(W_x, W_y, W_\theta)$  are the search window sizes,  $\text{INT}$  denotes the rounding function, and  $\oplus$  denotes the matrix sum.

Rough mapping is the process of inserting scans into blocks at optimal poses. Using the best estimated poses, the global map is constructed by aligning a sequence of scans and blocks (Thrun et al., 2000). Therefore, a rough map consisting of a sequence of blocks can be represented as:

$$m = \left\{ (B_1, \xi_{B_1}^W), (B_2, \xi_{B_2}^W), \dots, (B_l, \xi_{B_l}^W), \dots, (B_L, \xi_{B_L}^W) \right\} \quad (17)$$

where  $m$  denotes the rough map,  $B_l$  represents a block,  $\xi_{B_l}^W$  is its pose in frame  $\{B\}$  with respect to  $\{W\}$ , as well as  $l$  denotes a block index.

### 2.3. Map correction for pose optimization (MCPO)

Although a global map is constructed in the rough mapping module, the accumulative errors caused by scan matching need to be further reduced. Thus, the goal of the MCPO model is to increase the capacity of the error-elimination strategy. The optimization-based method has been reported to be effective for the eliminating accumulative error in the

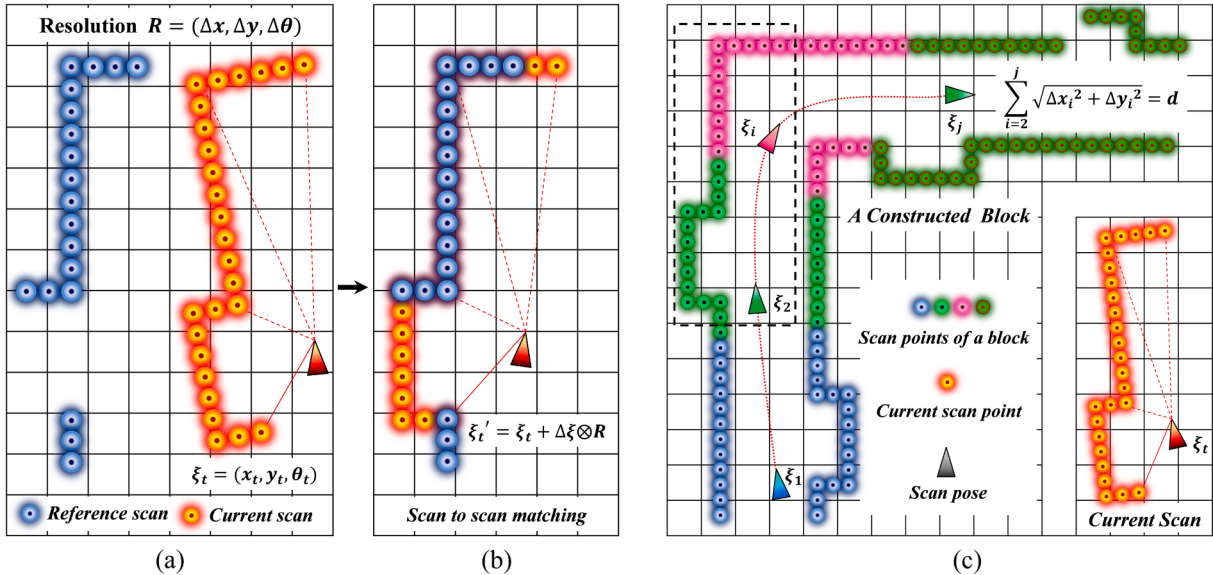


**Fig. 5.** A graphical illustration of the construction of a block and scan-to-block matching, (a) the probability distributions of the reference and current scan points (the probability is visualized as a circle with a color gradient, and the value decreases outward from the center of the circle), (b) scan-to-scan matching, (c) examples of the construction of a block and scan-to-block matching (this block consists of a collection of consecutive scans within a given moving length  $d$ , and the matching region of current scan and block is displayed within the black dotted rectangle).

process of mobile mapping (Konolige et al., 2010; Carbone et al., Jun 2014). In our approach, a local map correction module is proposed to optimize the rough map as much as possible. Using the results of the local map correction as constraints, the global pose optimization module is implemented, significantly eliminating the cumulative error. The final optimal state of the MCPO model is a global, consistent map with high accuracy. The process of the MCPO model can be expressed in Fig. 6.

### 2.3.1. Block based local map correction

As the errors caused by scan matching over long periods of time, there is some drift in the constructed rough map, which results in some gaps between the blocks in the loop closure. The gap is illustrated in Fig. 6(a) and (b). Our method tends to remove the gaps of blocks to correct the rough map as much as possible.

For such an optimization problem, the quality of the optimization result has been demonstrated to strongly depend on the quality of the constraint (Konolige et al., 2010). In addition, loop closure detection has been used to construct constraints for this optimization problem (Hess et al., 2016). Nevertheless, the scenarios with few features and similar components also degrade the performance of loop closure detection, like data association. To address the problem, a block-to-block matching strategy is proposed for loop closure detection, as shown in Fig. 7. First, based on the constructed rough map, consisting of a sequence of blocks, the relative poses where scans are inserted into the blocks are recorded for use in the loop closing optimization. Next, all the block pairs consisting of two blocks are considered for loop closing, except for adjacent blocks that have been matched in the rough mapping module. Then, scan matching is repeatedly performed between the current block and the preceding reference block to find the maximal probabilities at the scan points. The block-to-block matching strategy is an additional improvement over the proposed scan-to-block matching approach. The implementation of block-to-block matching is based on the triple-resolution probability grid ( $R_1, R_2, R_3$ ) and the search window ( $W_x, W_y, W_\theta$ ), which is similar to scan-to-block matching. However, we instead implement scan matching between two blocks. Accordingly, the optimization problem of block-to-block matching can be written as:

$$\underset{\xi_{B_C}^W}{\operatorname{argmin}} \sum_{i=1}^N \left( 1 - P \left( \left\{ z'_1, z'_2, z'_3, \dots, z'_j \right\}_{z'_j \in B_C^l} \middle| \xi_{B_C}^W, B_R \right) \right)^2 \quad (18)$$

$$\text{index}(B_C) - \text{index}(B_R) \neq 1 \quad (19)$$

where  $B_R$  and  $B_C$  denote the preceding reference block and current block,  $\xi_{B_C}^W$  is the currently estimated pose,  $N$  is the number of scan points contained in current block, and  $\text{index}$  denotes the operation of obtaining the index.

Moreover, based on block matching, the local map correction constraints can be constructed between blocks. The error caused by scan matching is mainly accumulated between consecutive blocks rather than scans stored in blocks. The block is used to construct map correction constraints and then rigidly transformed to correct the map as much as possible. If a good enough match is found between two blocks (i.e.,  $B_i$  and  $B_j$ ), the common points are set in matched blocks. For a pair of corresponding scans (i.e.,  $s_i^p$  and  $s_j^q$ ) contained in  $B_i$  and  $B_j$ , the actual positions of the scan points are  $H_i^p = (x_i^p, y_i^p)$  and  $H_j^q = (x_j^q, y_j^q)$ , respectively, and the measured positions based on loop closure detection are denoted  $h_i^p$  and  $h_j^q$ . The map correction constraint can be expressed as follows:

$$\text{Index}_f = \{(m, n)_f\} = \left\{ (m, n)_f \mid h_i^p(m) = h_j^q(n) \right\}_{f=1,2,\dots,F} \quad (20)$$

$$CP_i^j = \{ [H_i^p(m), H_j^q(n)] \} \quad (21)$$

$$R_{\xi_i^j}^f = \sqrt{(x_i^p(m) - x_j^q(n))^2 + (y_i^p(m) - y_j^q(n))^2} \quad (22)$$

where  $CP_i^j$  is the common point between block  $B_i$  and block  $B_j$ ,  $D$  denotes the distance between two points,  $f$  is the index of the common point, and  $R_{\xi_i^j}^f$  denotes the residual of Euclidean distance between common points given the current relative pose between blocks  $B_i$  and  $B_j$ , which can be used as constraints for local map correction. The constraints are described in Fig. 6(c). Subsequently, the block-based constraints are added to the map optimization problem. The local map correction is formulated as a nonlinear least squares problem, which can be expressed as follows:

$$\underset{\psi_i^j}{\operatorname{argmin}} \sum_{ij} \sum_{f=1}^F \left( R_{\xi_i^j}^f \right)^2 \quad (23)$$

where  $\psi_i^j$  is the optimal relative pose of the blocks, and  $F$  is the number of constraints for a block. The map correction is shown in Fig. 6(d).

### 2.3.2. Global pose optimization using map constraints

Although a local map correction module is proposed to optimize the map, the corrected map is limited to the blocks with loop closing constraints, and needs to be globally optimized. A global pose optimization module is proposed to optimize all poses of the scans and blocks, following the sparse pose adjustment (SPA) approach (Konolige et al., 2010). More importantly, the relative poses of blocks that are accurately obtained from the local map correction module are added to the global pose optimization problem as crucial constraints, as shown in Fig. 6(e). The aim is to enhance the global pose optimization performance in eliminating accumulated error. The global pose optimization, like local map correction, is also regarded as a nonlinear least squares problem, which can be expressed as:

$$\begin{cases} \underset{\xi^s, \xi^B}{\operatorname{argmin}} \frac{1}{2} \sum_{mn} \rho(E^2(\xi_m^s, \xi_n^B, \Sigma_{mn}, \psi_m^n)) \\ E^2(\xi_m^s, \xi_n^B, \Sigma_{mn}, \psi_m^n) = e(\xi_m^s, \xi_n^B, \psi_m^n)^T \Sigma_{mn}^{-1} e(\xi_m^s, \xi_n^B, \psi_m^n) \\ e(\xi_m^s, \xi_n^B, \psi_m^n) = \psi_m^n - \begin{pmatrix} R_{\xi_n^B}^{-1}(t_{\xi_n^B} - t_{\xi_m^s}) \\ \xi_\theta^B - \xi_\theta^s \end{pmatrix} \end{cases} \quad (24)$$

where  $\xi^s = \{\xi_m^s\}$  and  $\xi^B = \{\xi_n^B\}$  represent the optimized poses of scans and blocks in frame  $\{W\}$ , respectively. For the pose optimization problem, the constraints consist of the relative pose  $\psi_m^n$  and covariance matrix  $\Sigma_{mn}$ .  $\psi_m^n$  denotes the pose of the scan of frame  $\{S\}$  with respect to  $\{B\}$ , which is provided by the output of the local map correction module. The associated covariance matrix  $\Sigma_{mn}$  can be computed based on the previous work in (Olson and IEEE, 2009). Furthermore, to reduce the adverse effect of mismatch on pose optimization, a Huber loss function  $\rho$  is used in our strategy to increase the robustness against the scenarios with few features and similar components. The final state of the global pose optimization is shown in Fig. 6(f).

## 3. Experiments

To evaluate the performance of the proposed method, mobile mapping experiments were conducted on the two different datasets. The evaluation criteria were used to assess the qualities of the experimental results. The performance of our approach was compared with those of five other state-of-the-art methods. Moreover, based on the constructed high-accuracy 2D map, 3D indoor modeling results of two problematic scenarios are presented in this section.

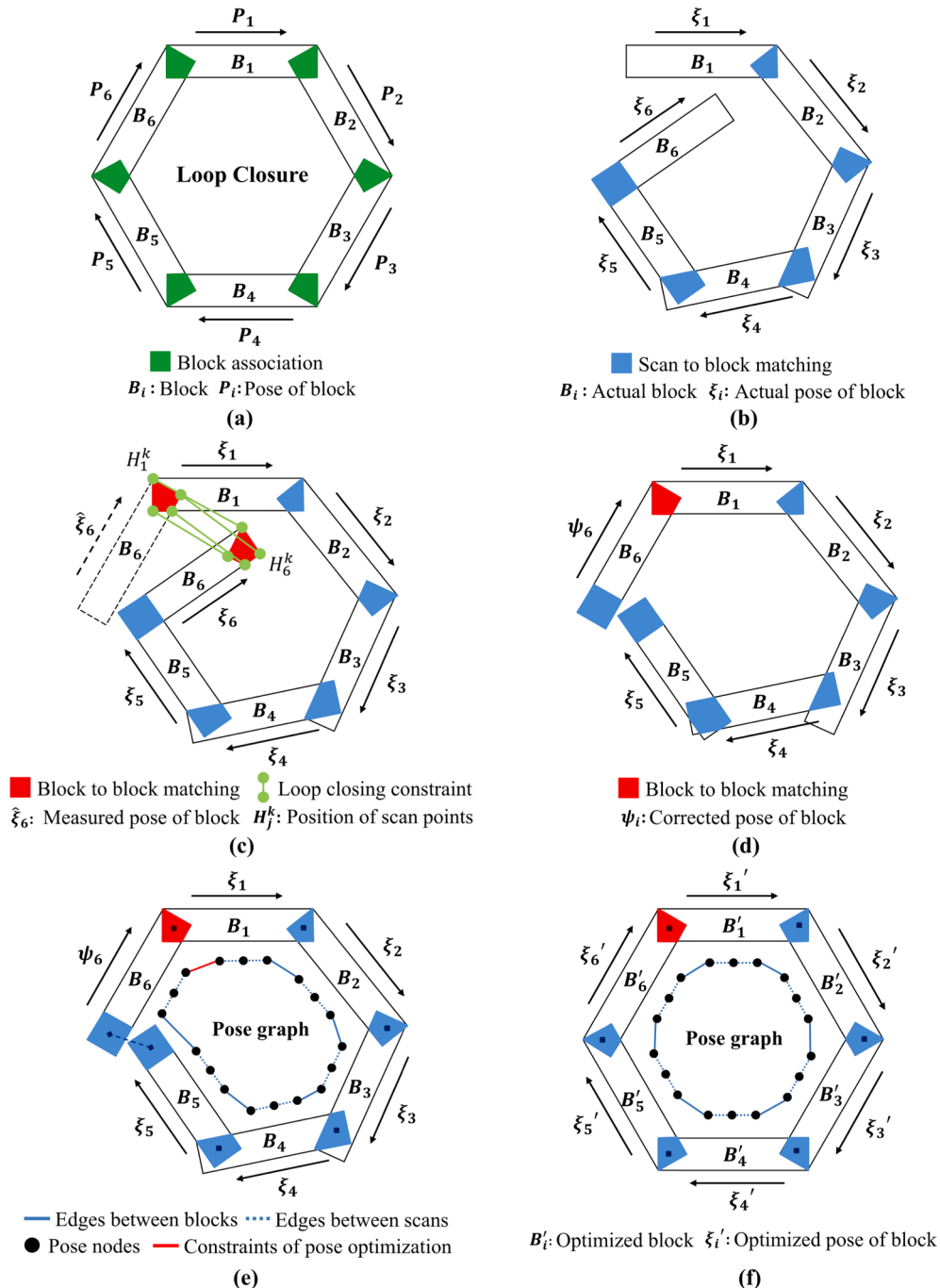


**Fig. 6.** A graphical illustration of the MCPO model, (a) the target of global mapping, (b) the actual state of rough mapping, (c) the constructed constraints used for local map correction, (d) the result of local map correction, (e) the global pose optimization based on the map constraints, (f) the final state of mapping.

### 3.1. Experimental scenarios and datasets

Two different problematic scenarios are used to build experimental datasets, as shown in Fig. 8. Table 1 lists the data specifications in the two studied scenarios. Scenario I and II are located on the campus of Tongji University, China. Scenario I is a long corridor that is characterized by similar structures and few features. There are only a few components in the scenario, such as walls and doors. The smooth walls are covered with plaster. The doors, which have the same size and texture, are symmetrically distributed on both sides in this scenario. This environment may make data association difficult and thus seriously influence SLAM-based mobile mapping. Scenario II is a large underground parking garage that contains cars and walls as well as pillars.

Many cars of the same size are parked neatly against the walls. In addition, a large number of pillars with the same shape and size are uniformly distributed in this scenario. Scenario II represents a large-scale environment that significantly influences back-end optimization and thus poses a great challenge to error elimination in the process of mobile mapping.

The datasets for scenarios I and II were captured by maneuvering a mobile platform equipped with a single-line LiDAR sensor and a low-cost IMU around the area. The LiDAR sensor (Hokuyo UTM-30LX) has a maximum effective range of 30 m with a range accuracy of  $\pm 30$  mm at 0.1 m-10 m and  $\pm 50$  mm at 10 m-30 m, and records data in an angle range of  $270^\circ$  with an angular resolution of  $0.25^\circ$  at 40 Hz. The IMU sensor (SBG Ellipse-A) contains a three-axis gyroscope and a three-axis

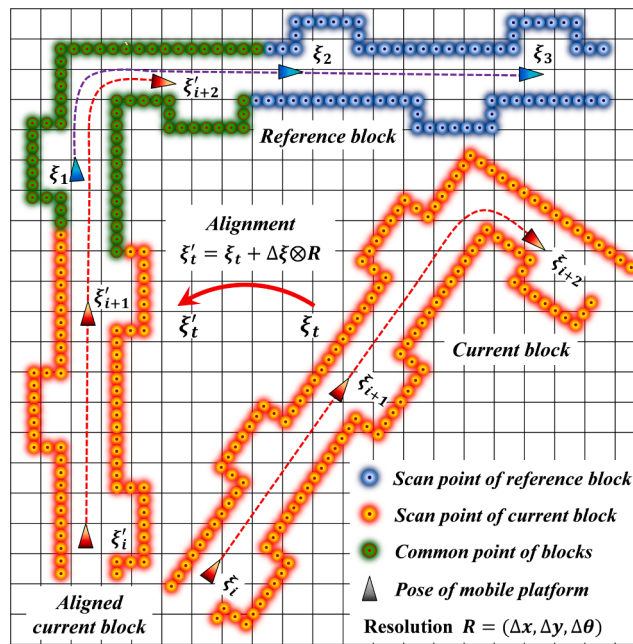


**Fig. 7.** A graphical illustration of the block-to-block matching. Scan matching is implemented between the reference and current blocks, and then the current block is aligned with the reference block at the best estimated poses.

accelerometer, with a sampling frequency of 200 Hz.

### 3.2. Evaluation criteria

To quantitatively assess the performance of our approach, ground-truth data of checkpoints for the trajectory and map were acquired to evaluate the accuracy of the pose computation and mapping (Wang et al., 2018; Wen et al., 2018). Using the total station, the ground-truth positions of checkpoints located in the trajectory of the mapping platform were obtained to verify the pose computation accuracy. There were 11 and 22 trajectory checkpoints for scenarios I and II, respectively. The angular accuracy and range accuracy of the total station used were  $2''$  and  $\pm(2.0\text{mm}+2 \times 10^{-6}*\text{D})$ , respectively, which were obviously higher than those of the LiDAR sensor. D denotes the observation distance of the total station. After data collection, the coordinate systems of the total station were transformed to match those of the LiDAR and IMU data. Moreover, the ground truth of the distance between two checkpoints (checkpoint pair) for the map was collected using a laser range finder with a range accuracy of  $\pm(2.0\text{mm}+5 \times 10^{-5}*\text{D})$  to test the mapping accuracy. Obvious fixed objects, such as the corners and walls of the building, were selected as the main checkpoint pairs for accuracy evaluation. There were 20 and 26 checkpoint pairs for the maps for

scenarios I and II, respectively.

After the ground-truth data were obtained, the performance of the proposed method was evaluated using five quantitative metrics, namely, closure error (CE), position error of the pose (PE), absolute map error (AME), relative map error (RME), and computation time (T). These quantitative metrics were calculated as follows:

$$CE = \sqrt{(x_{\text{ini}} - x_{\text{end}})^2 + (y_{\text{ini}} - y_{\text{end}})^2} \quad (25)$$

$$PE_i = \sqrt{\left(x_i - \bar{x}_i\right)^2 + \left(y_i - \bar{y}_i\right)^2}_{(i=1,2,\dots,I)} \quad (26)$$

$$AME_j = \text{abs}\left(d_j - \bar{d}_j\right)_{(j=1,2,\dots,J)} \quad (27)$$

$$RME_j = AME / \bar{d}_{(j=1,2,\dots,J)} \quad (28)$$

where  $(x_{\text{ini}}, y_{\text{ini}})$  and  $(x_{\text{end}}, y_{\text{end}})$  are the positions of the initial and end points, respectively.  $(x_i, y_i)$  and  $(\bar{x}_i, \bar{y}_i)$  denote the actual and ground-truth positions of the checkpoint for the trajectory, respectively.  $d_j$  and  $\bar{d}_j$  represent the actual and ground-truth distances of the checkpoint pair for the map, respectively. I and J are the numbers of trajectory checkpoints and map checkpoint pairs, respectively. The CE and the PE are used to assess the accuracy of the pose computation. The AME and RME are used to verify the mapping accuracy. More importantly, both the mean and root mean square (RMS) of the PE, AME and RME, are computed to evaluate the overall performance of pose computation and mapping. To assess the complexity of the method, all the experiments were conducted by means of a computer containing an Intel single core i7-8700K CPU and 16 GB of RAM to measure the computation time.

### 3.3. Results and assessment

The experiments conducted on the two different datasets followed the same processing scheme. The proposed method has three groups of key parameters: the resolutions of probability grids (*i.e.*,  $R_1, R_2, R_3$ ), the given length of the block (*i.e.*,  $d$ ), and the number of constraints for each pair of matched blocks (*i.e.*,  $F$ ). The detailed results of a sensitivity analysis on these parameters and the optimal values are given in Section

**Table 1**

Data specifications.

Study area	Scenario 1	Scenario 2
Size of scenario	2.4 m × 135.4 m	58.6 m × 126.4 m
Number of points	45,681,623	54,817,516
Time of travel	17.68 min	21.23 min
Length of travel	282 m	602 m

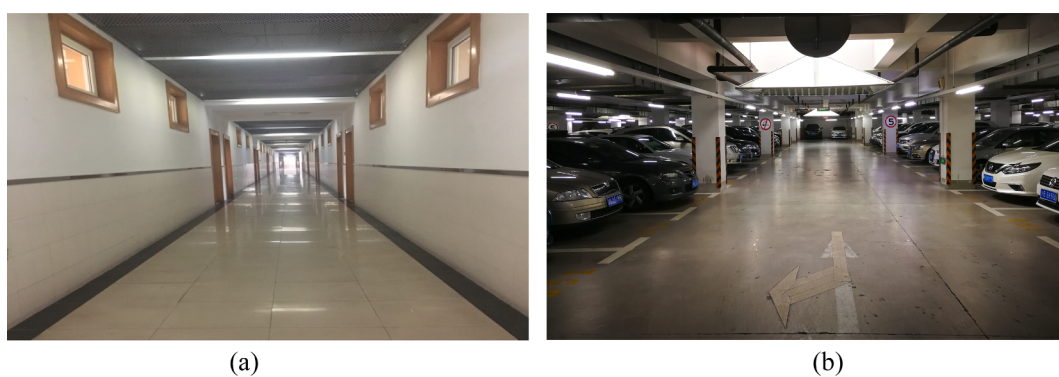


**Fig. 8.** Examples of experimental scenarios: (a) scenario I (the long corridor) and (b) scenario II (the large underground parking garage).

## 4.

The pose computation results for scenarios I and II are shown in Fig. 9. Here, the CE and the checkpoints obtained for two scenarios are used to visually assess the pose accuracy. For scenarios I and II, the drifts of the initial pose and the PCRM pose increase with the movement of the mapping platform due to error accumulating over time. According to Fig. 9(a), a large drift in the IMU data occurs in scenario I; thus, the initial poses are far from the checkpoints. Compared with the initial poses, the PCRM poses are closer to the checkpoints, while the CE is still large. The results show that the PCRM model overcomes the problems of few features and similar components in scenario I using the initial poses, and outputs relatively accurate poses. Based on the PCRM poses, the resulting poses of the MCPO model are basically in accordance with the checkpoints, and the poses are closed visually. The results indicate the capability of the MCPO model to eliminate cumulative error. For scenario II, the initial poses are similar to those of scenario I. In particular, the results of the PCRM model in Fig. 9(b) show more serious drift than the initial poses. This is mainly because the cumulative error caused by scan matching is more significant in large-scale environments. In addition, the MCPO poses of scenarios I and II follow the same pattern. Thus, the performance of the MCPO model for eliminating cumulative error is considered satisfactory in the large-scale scenario.

A rough map was constructed based on the PCRM model, and then the final map was obtained using the MCPO model. The mapping results for scenarios I and II are shown in Figs. 10 and 11, respectively. In the results, the rough maps completely cover the environmental components, such as the doors and walls in scenario I as well as the pillars and walls in scenario II. However, there are some drifts and gaps in the rough maps for scenarios I and II, due to cumulative error and repeated measurements. The results indicate the requested performance of the PCRM model for rough mapping in problematic environment. Moreover, Fig. 10(b) and Fig. 11(b) clearly show that the drifts and gaps in the rough maps of the two scenarios are removed. There are distinct features such as clear corners and straight lines, and various components with clear outlines such as walls, doors, stairs and pillars, in the scenarios. Thus, the resulting maps of the MCPO model accurately present the boundaries, components and features of scenarios. The results also demonstrate the capacity of the MCPO model for eliminating cumulative error. Therefore, the proposed method can achieve satisfactory performance regarding constructing consistent maps in problematic scenario.

The quantitative assessment of the pose computation results for scenarios I and II are shown in Fig. 12(a) and (b), respectively. The PE of each checkpoint and the CE express the pose accuracy. The pose computation results for these two scenarios followed the same pattern. Due to error accumulating over time, the PE of the checkpoint increases with increasing trajectory length, and the CEs of the PCRM poses are large. The statistical assessment results obtained for scenarios I and II are shown in Table 2. In the results of the MCPO model for scenarios I and II, the CEs are 0.0130 m and 0.0048 m, respectively; for PE, the mean errors are very close to the RMS errors, which are 0.07 m and 0.05 m in scenarios I and II, respectively. In particular, the PEs of the checkpoints that are close to the beginning and ending of poses are smaller. Thus, the pose accuracy was significantly improved by the MCPO model, and the effect of the MCPO model was more obvious near beginning and ending of poses due to the constructed loop closing constraints. Another objective of quality assessment was to evaluate the accuracy of the map. The quantitative assessment of mapping results for scenarios I and II are shown in Fig. 13(a) and (b), respectively. The statistical results are shown in Table 2. In terms of the mean and RMS errors of the final maps, the AME and RME for scenario I are approximately 0.008 m and 0.1%, respectively, and the AME and RME for scenario II are approximately 0.012 m and 0.2%, respectively. Moreover, for mobile 2D mapping, there is no universal standard for high-accuracy 2D maps. However, according to the published results in (Hess et al., 2016), the mean and RMS of RME should be below 0.6%. Based on these criteria, the mapping results for scenarios I and II were considered highly accurate.

## 3.4. Comparison

The performance of the proposed method was further evaluated by comparing the results with those of other published methods. The other methods, 2D SLAM<sup>1</sup>, Cartographer<sup>2</sup> (Hess et al., 2016), LTDE (Wang et al., 2018), CNC (Wen et al., 2018) and LSO (Ren et al., 2019), were implemented. 2D SLAM is a classic 2D LiDAR-based SLAM method, that is based on a double-resolution scan-to-scan matching strategy. Cartographer is a well-performing 2D mapping method, in which scan-to-map matching is used for data association and loop closure optimization to reduce cumulative error. The methods of 2D SLAM and Cartographer have been publicly available in the GitHub community. Additionally, the CNC method is based on a double-resolution probability grid and adds a distance constraint into back-end optimization to improve the mapping accuracy. To perform CNC, 8 and 10 distance constraints were added for scenarios I and II, respectively. The mapping method of LTDE, in which EKF is used to achieve sensor fusion of LiDAR and IMU, is designed for low-texture and dynamic environments. LSO is also a well-performing mapping method, in which the double-resolution correlative scan matching algorithm is particularly improved for large-scale environments. Considering that the features used by LSO are few in the problematic environment, we instead extracted the point and line features for loop closure detection. These methods were repeatedly performed with different parameter settings to achieve the best mapping performance. Moreover, for effective accuracy evaluation of mapping, the mapping results of the other methods were transformed to the form of point clouds by aligning all scans based on the computed poses.

The comparative results of pose computation for different mapping methods are described in Fig. 14. It can be clear that the poses of our method for scenarios I and II are basically in accord with the checkpoints, which outperforms the other methods due to smaller CE. The LTDE and the LSO also perform well in scenarios I and II, and achieve results close to that of the proposed method. As seen in Fig. 14 (a), the poses of the 2D SLAM and the Cartographer have significant drifts in scenario I. For the results of the CNC in Fig. 14(a) and (b), the resulting poses for scenarios I and II have some drifts and are far from the checkpoints. Moreover, the comparative mapping results of different methods for scenarios I and II are shown in Figs. 15 and 16, respectively. Compared with 5 other methods, our method presents clearer boundaries of scenarios, and achieves better consistency of maps. As can be seen from Fig. 15(a) and (b), the 2D SLAM and the Cartographer have failed in mapping for scenario I. There are several significant drifts and gaps in the resulting maps of the CNC, LTDE and LSO, as shown in Fig. 15(c), (d) and (e). Considering the mapping results shown in Fig. 16, other methods have constructed relatively consistent maps for scenario II, but some gaps were still contained in the maps, especially for the CNC results.

The quantitative comparisons for six mapping methods, and for all evaluation criteria are shown in Table 3. The proposed method yields the best results in scenarios I and II, achieving the minimum values in terms of both pose and map performance measures among all the test methods. The main reason is that the proposed method adopts the PCRM model to reduce the uncertainty of pose and encodes more information for improving rough mapping in the similar-component and featureless scenario, and uses the MCPO model to significantly eliminate cumulative error in the large-scale scenario. In these two experiments, the LTDE and LSO methods achieve relatively satisfactory performances in scenarios I and II. The possible reason is that the IMU sensor is used in these two methods to provide the initial pose for data association, which validates that the initial pose can effectively improve the robustness of data association. It is noteworthy that the LSO method performs better than the LTDE method in scenario II. This reason could be that the LSO

<sup>1</sup> 2D SLAM: <https://github.com/meyiao/LaserSLAM>.

<sup>2</sup> Cartographer: <https://github.com/cartographer-project/cartographer>.

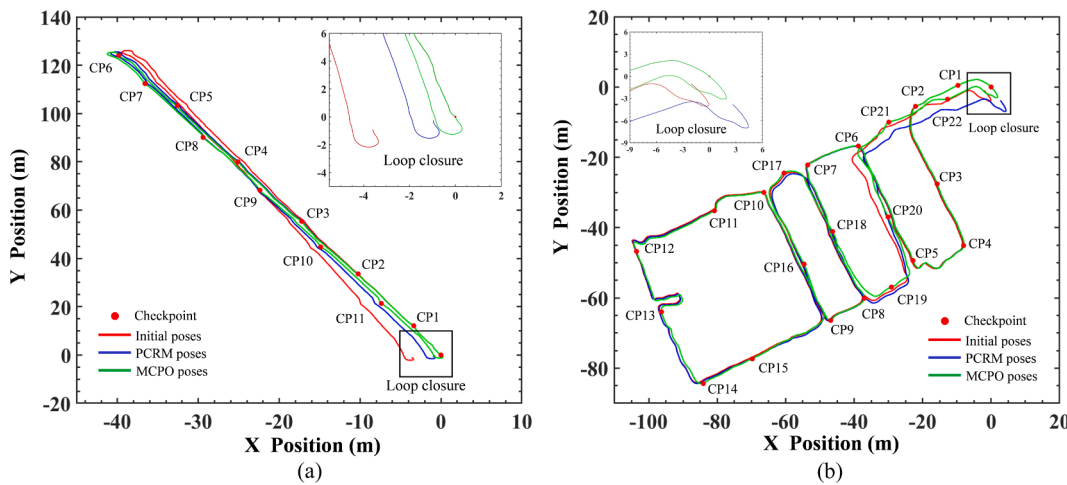


Fig. 9. The pose computation results: (a) scenario I, (b) scenario II.

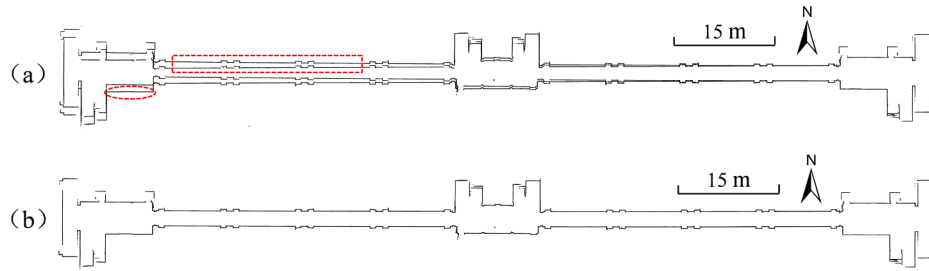


Fig. 10. The mapping results for scenario I, (a) the rough map of the PCRM model (examples of drift and a gap are depicted in the red ellipse and rectangle, respectively), and (b) the final map of the MCPO model. (For interpretation of the references to color in this figure legend, the reader is referred to the web version of this article.)

method extracts more robust features for loop closure detection and validation, which could achieve better performance in eliminating cumulative error than the LTDE method, especially in large-scale scenarios. In contrast, the 2D SLAM and Cartographer methods consistently provide the worst results in scenario I. The reason for the poor performance is that the scenarios with few features and similar components result in few distinctive features in LiDAR scans and no obvious changes between two consecutive scans, which could make data association difficult (Wang et al., 2018; Wen et al., 2018). In this case, these two methods are independent of the initial pose provided by IMU data, and thus, the scenarios with few features and similar components significantly degrades the performance of data association, leading to large drift in their results. In the experiment of scenario II, the Cartographer method performs better than the 2D SLAM method. The issue could be explained by the fact that loop closure detection of the Cartographer method, which is based on scan-to-map matching, could effectively eliminate cumulative error, especially in the large-scale scenario. With regard to the CNC method, its performance is moderate in scenario I. One reason for the result in scenario I is that the initial pose is provided by the IMU sensor to improve the robustness of data association. The other is that the distance measurement of the control network is added as a stable geometric constraint into back-end optimization against the scenarios with few features and similar components. It is worth noting that the CNC method presents the worst result in scenario II. The possible reason for the poor performances is that the number of distance constraints could not be enough to effectively eliminate cumulative error due to the limit of prior control network, compared with that of other back-end optimization methods that are based on scan matching. In addition, the distance constraint of the CNC method considers only the location ( $x, y$ ) of the pose without the orientation  $\theta$ . This could degrade the quality of cumulative error elimination, as both location

and orientation are involved in back-end optimization. In addition to the computation time  $T$ , the proposed method cost a moderate level of computation time among the compared methods.

### 3.5. Application to 3D indoor modeling

Based on the constructed high-accuracy 2D map, a wireframe extraction method, namely, ring-stepping clustering (Wu et al., 2019), was employed to automatically obtain a 2D wireframe of the scenario. Moreover, the build height information was accurately acquired using a laser rangefinder, and then wireframe stretching was implemented for indoor scenario modeling. The high-accuracy build modeling results of scenarios I and II are shown in Fig. 17.

The building models of scenarios I and II are visualized in 3D, and the boundaries, ranges and complexities are expressed clearly. In the building models, various structural components such as walls, doors and pillars, are also presented in 3D, and their shapes, sizes and positions can be obtained accurately. Thus, the modeling results can not only accurately present geometric and structural information of the complex scenarios in 3D, but also convey rich component information. Moreover, compared with some significant works in 3D indoor modeling, such as Wang's study in (Wang, 2018), the details of our building modeling need to be further improved. For example, although the positions and widths of the doors could be accurately obtained, their heights could not be covered in our modeling results. However, our method has the advantages of higher accuracy and computational efficiency, which can achieve efficient and accurate indoor modeling. Therefore, the proposed method can be considered satisfactory in practical applications.

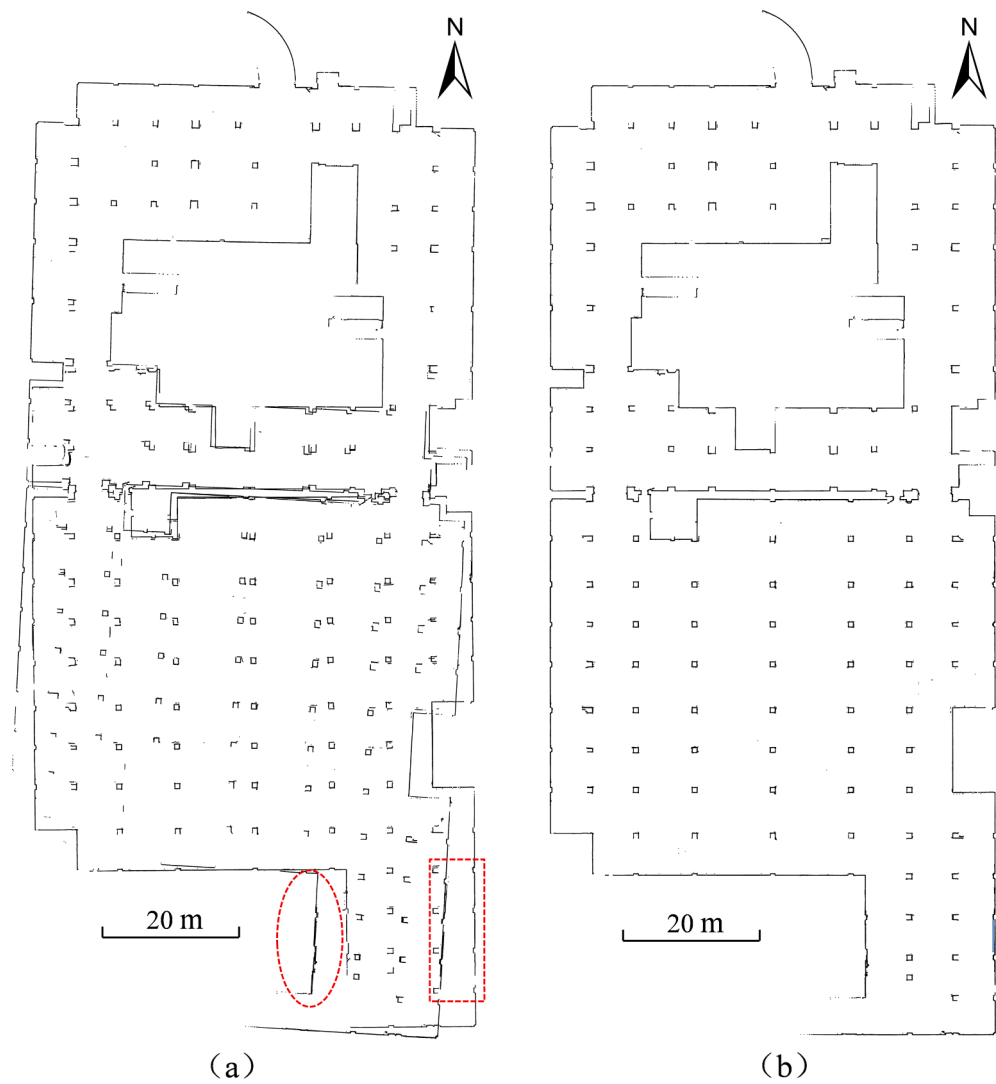


**Fig. 11.** The mapping results for scenario II, (a) the rough map of the PCRM model (examples of drift and a gap are depicted in the red ellipse and rectangle, respectively), and (b) the final map of the MCPO model. (For interpretation of the references to color in this figure legend, the reader is referred to the web version of this article.)

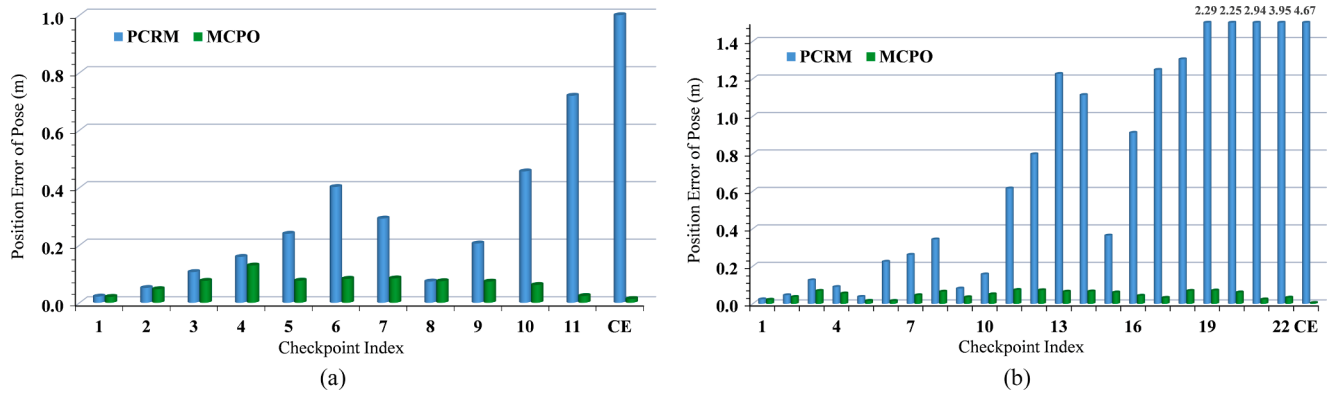


**Fig. 12.** Assessment of pose computation results: (a) scenario I, (b) scenario II.

#### 4. Discussion

#### 4.1. Influence of the probability grid resolution

As stated above, the resolution of the probability grid is an important

characteristic. It has a significant impact on the precision of scan matching and the computation cost and thus influences the quality of mapping. To evaluate the influence of the grid resolution, the proposed method was repeatedly performed on 10 groups of probability grids of different resolutions. The resolution settings of the different probability

**Table 2**

Statistical assessment results.

Metrics	CE (m)	Mean PE (m)	RMS PE (m)	Mean AME (m)	RMS AME (m)	Mean RME	RMS RME
Scenario I	0.0130	0.0684	0.0743	0.0071	0.0085	0.0011	0.0014
Scenario II	0.0048	0.0494	0.0530	0.0113	0.0126	0.0022	0.0025

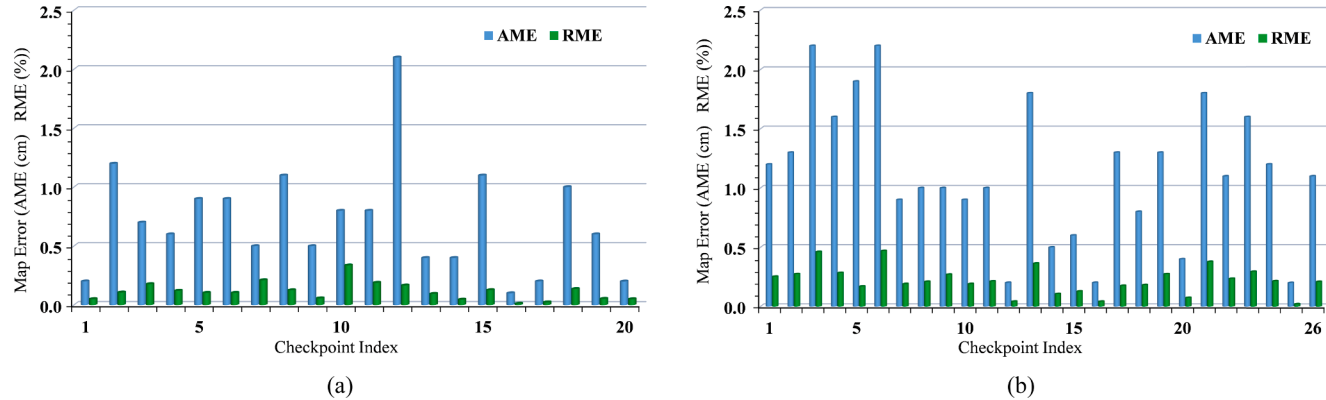


Fig. 13. Assessment of mapping results: (a) scenario I, (b) scenario II.

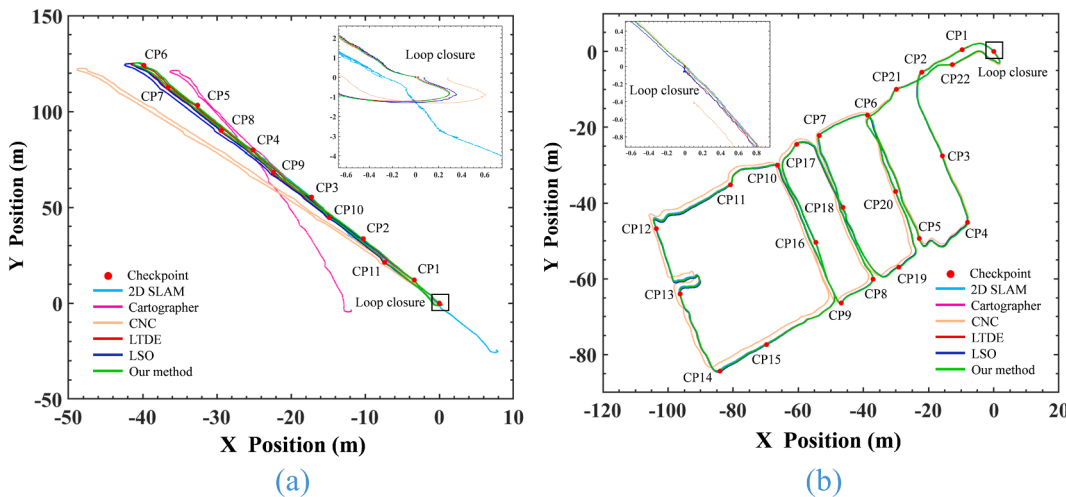


Fig. 14. The pose computation results of other methods and the proposed method: (a) scenario I, (b) scenario II.

grids are described in Table 4, where  $R_1, R_2, R_3$  denote rough, middle and fine resolutions, respectively. The first group describes the single-resolution grid, and the second is the double-resolution grid. The others present triple-resolution grids with different resolutions. During the evaluation, the CE and T are used to assess the influence of the grid resolution on the mapping performance.

The evaluation results for scenarios I and II are shown in Fig. 18. Fig. 18(a) clearly shows that the first grid, which is a single-resolution grid with high resolution, results in the smallest CE but the largest T. In addition, the multi-resolution grids with high resolution, such as the second and third group of grids, achieve the smallest CE but with lower computation cost. When the resolution is lower than that of third group of grids, the CE increase and T is almost constant because the precision of scan matching significantly decreases. Similar to the result of scenario I, the performance of the third group of probability grids in scenario II is considered satisfactory due to relatively lower CE and T. Thus, the triple-resolution grid offers better performance than the single-resolution and double-resolution grids regarding the computation cost, and high resolution significantly increases the mapping accuracy. Based on the discussion above, the optimal resolution for the probability grid is the third

group in Table 4.

#### 4.2. Parameter influence

In our method, the mapping performance strongly depends on the results of block construction. Specifically, the given length of the block  $d$  is an important parameter in the rough mapping module because it determines the quality of scan-to-block matching and the computation cost. To test the sensitivity to this parameter, the proposed method was executed repeatedly with different block lengths (*i.e.*,  $d$ ) on two datasets corresponding to scenarios I and II. Six values of  $d$  were uniformly sampled between 1 and 6 m. The quantitative metrics, such as the mean score in Eq. (11), which directly presents the quality of the scan matching, and T, were calculated to assess the influence of  $d$ .

The assessment results for scenarios I and II are shown in Fig. 19. Both curves for scenarios I and II follow the same pattern, and the evaluation metrics are maintained at a good level within a certain range of  $d$ . When the value of  $d$  is small, the number of blocks increases and the information stored in block decreases, hence decreasing the quality of the scan matching and increasing the computation complexity. Thus, the

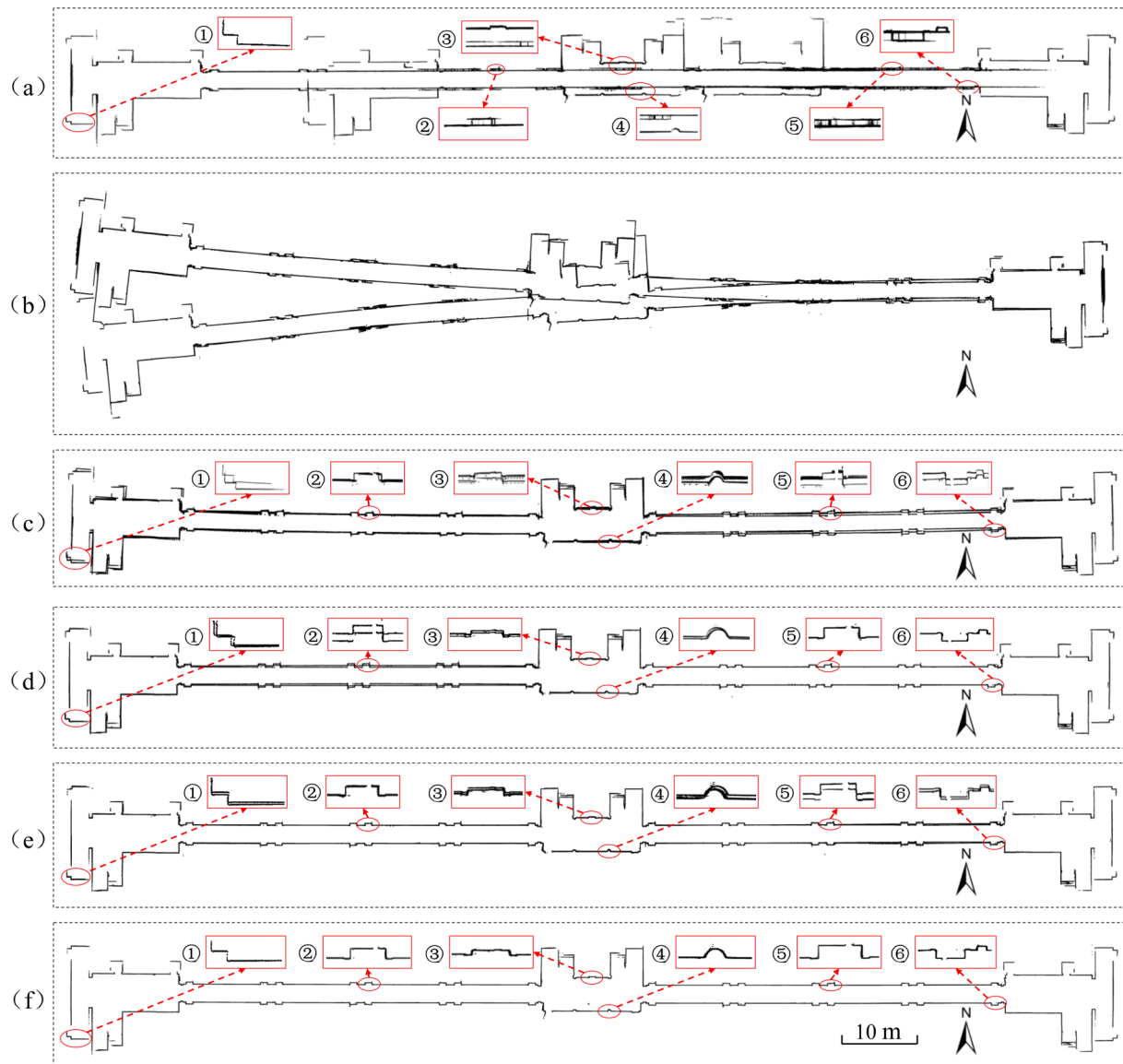


**Fig. 15.** The mapping results for scenario I of other methods and the proposed method, (a) 2D SLAM, (b) Cartographer, (c) CNC, (d) LTDE, (e) LSO, (f) the proposed method.

metric of the mean score is low and  $T$  is high. In addition, the quality of scan matching increase and the computation cost decrease with increasing  $d$ . When  $d$  becomes larger than 5 m, the mean score of scan matching begins to decrease because the errors caused by scan matching and the observation model easily accumulate over long periods of time, which may deteriorate the accuracy of the block. Therefore, considering the quality of the block and computation cost, the parameter  $d$  is set to 5 m in our implementation.

#### 4.3. Constraint influence

In the proposed method, the quality of the local map correction significantly influences the quality of the MCPO model. Particularly, the number of constraints for each pair of matched blocks (*i.e.*,  $F$ ) is an essential parameter that can determine the performance of the local map correction module and thus influences the quality of mapping. To assess the influence of the parameter, our method was repeatedly with eight values of  $F$  between 1 and 8 for scenarios I and II. In addition to the assessment metrics, the mean residual of all constraints ( $R$ ) in Eq. (22) was introduced to evaluate the performance of the local map correction

module, and CE was used for assessing the mapping quality.

Fig. 20 shows the influence of the number of constraints on the mapping quality for scenarios I and II. Our method yields satisfactory performance within a certain range of  $F$ , and the results for scenarios I and II follow a similar trend. According to the results for various radius  $F$ , a small value results in a high CE and  $R$  due to the local minimum in the optimization problem. As  $F$  becomes larger, the local map is better corrected, so the CE and  $R$  significantly decrease. When  $F$  becomes larger than 4, the values of CE and  $R$  tend to remain constant, mainly because the number of constraints for each pair of matched blocks is enough to compute the globally optimal solution for local map correction. Thus, the optimal value for  $F$  is 4 in scenarios I and II.

#### 4.4. Inapplicable conditions

Considering that the capacities of data association and cumulative error elimination can be significantly improved in the PCRM and MCPO models, the proposed method can overcome the problematic scenarios and construct high-accuracy 2D mapping. The performance of the proposed method was evaluated in two problematic scenarios (long

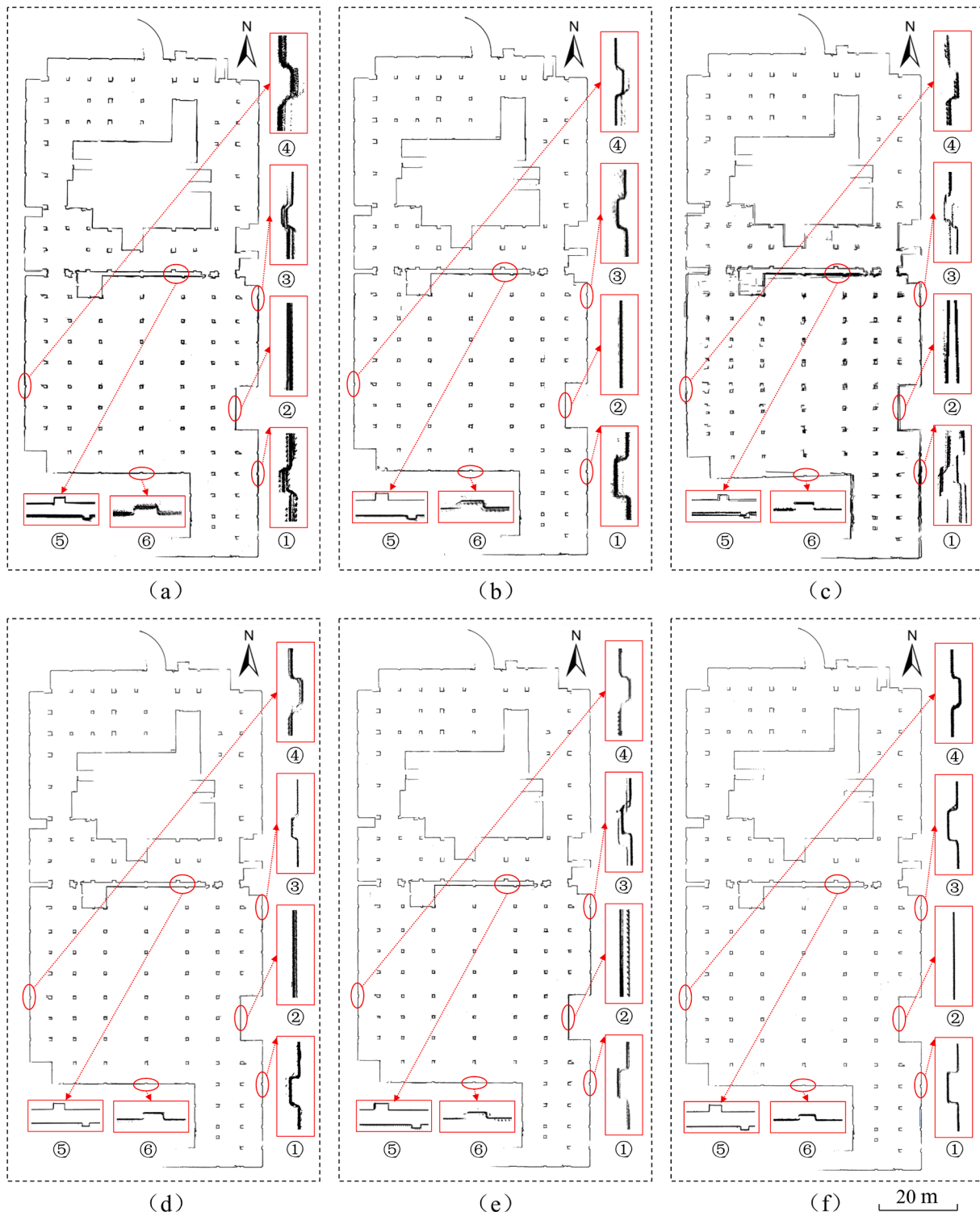


**Fig. 16.** The mapping results of other methods and the proposed method for scenario II, (a) 2D SLAM, (b) Cartographer, (c) CNC, (d) LTDE, (e) LSO, (f) the proposed method.

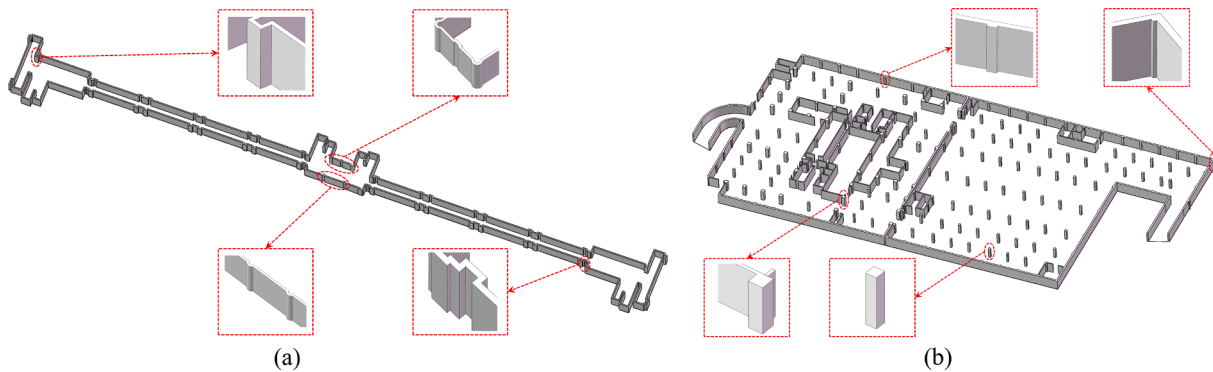
corridor and large underground parking garage). We also consider that the proposed method can be well applied to the scenario with glossy tile because it has little influence on the geometric observations of the LiDAR sensor. However, some special specular surfaces, such as a mirror and a transparent glass, significantly influence the quality of the LiDAR data collection. Thus, when the specular surface is complex, such as a mirror or a transparent glass, the LiDAR sensor could be ineffective, and thus our method becomes inapplicable.

The behavior of the proposed method for occlusions and dynamic objects is another issue worth discussing. In practical application, the occlusions and dynamic objects may degrade the performance of the proposed method, due to significant influence on data collection and data association. In the process of the data collection, the occlusions, including static and dynamic objects, are wrongly viewed as the boundary of scenario. Moreover, although the initial pose is estimated for data association to improve the robustness of the proposed method in

**Table 3**

Comparison of our method with five other advanced mapping methods for scenarios I and II (CE (cm), PE (cm), AME (cm), and T (min)).

Methods	Scenario I							Scenario II								
	CE	Mean PE	RMS PE	Mean AME	RMS AME	Mean RME	RMS RME	T	CE	Mean PE	RMS PE	Mean AME	RMS AME	Mean RME	RMS RME	T
2D SLAM	2560	2831	3270	7.05	11.59	1.09%	1.75%	10.8	0.94	16.22	20.50	5.23	6.03	1.00%	1.23%	18.2
Cartographer	1237	420.4	483.7	9.42	13.35	1.35%	1.89%	11.7	0.36	10.16	11.06	2.42	2.80	0.45%	0.56%	18.6
CNC	28.43	324.6	382.2	5.22	6.08	0.83%	1.03%	4.5	42.12	99.91	110.9	5.91	7.02	1.12%	2.19%	7.1
LTDE	3.43	22.33	25.01	3.33	4.75	0.65%	1.12%	5.8	4.90	7.94	8.62	3.39	3.90	0.66%	0.77%	10.5
LSO	7.86	62.07	74.78	2.55	3.82	0.57%	1.34%	5.3	5.63	15.99	17.28	3.62	5.00	0.68%	0.84%	9.4
Our method	<b>1.30</b>	<b>6.84</b>	<b>7.43</b>	<b>0.71</b>	<b>0.85</b>	<b>0.11%</b>	<b>0.14%</b>	<b>4.7</b>	<b>0.48</b>	<b>4.94</b>	<b>5.30</b>	<b>1.13</b>	<b>1.26</b>	<b>0.22%</b>	<b>0.25%</b>	<b>8.8</b>

**Fig. 17.** The 3D indoor modeling results for scenarios I and II, (a) scenario I, (b) scenario II.**Table 4**

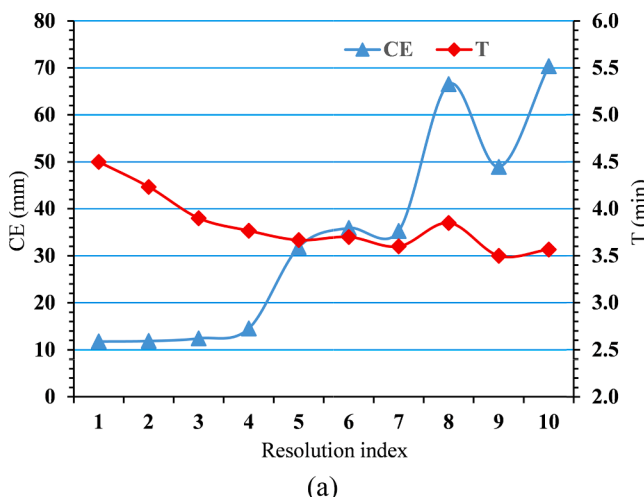
The resolution setting of the probability grids.

Resolution index	$R_1$		$R_2$		$R_3$	
	$\Delta x$ , y(m)	$\Delta\theta$ (rad)	$\Delta x$ , y(m)	$\Delta\theta$ (rad)	$\Delta x$ , y(m)	$\Delta\theta$ (rad)
1	0.01	0.01	0.01	0.01	0.01	0.01
2	0.01	0.01	0.02	0.01	0.02	0.01
3	0.01	0.01	0.02	0.01	0.04	0.01
4	0.01	0.01	0.04	0.01	0.08	0.01
5	0.03	0.01	0.06	0.02	0.1	0.05
6	0.03	0.01	0.06	0.02	0.12	0.05
7	0.03	0.01	0.08	0.02	0.14	0.05
8	0.05	0.02	0.08	0.03	0.16	0.10
9	0.05	0.02	0.10	0.03	0.18	0.10
10	0.05	0.02	0.10	0.03	0.20	0.10

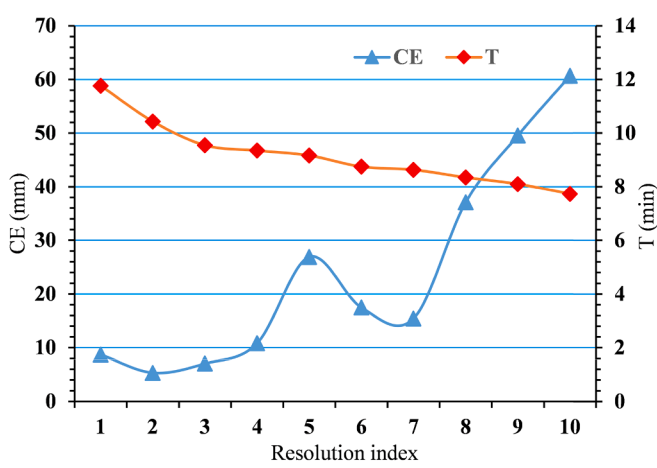
the problematic scenarios, our method may become inapplicable in the dynamic environment with a lot of moving objects due to significant influence on the data association.

## 5. Conclusion

In this paper, a cross-correction LiDAR SLAM method is proposed based on the mutual promotion of pose and map. The aim is to construct a high-accuracy 2D map for problematic scenario. The proposed method takes the cross correction between pose and map into account to enhance the data association and cumulative error elimination capacities. More specifically, with the assistance of the initial pose correction, the data association capacity can be increased, improving the rough mapping result, especially for scenarios with few features and similar components. Moreover, to increase the cumulative error elimination capacity, constraints are constructed from the map in our study and



(a)



(b)

**Fig. 18.** Influence of the resolution of the probability grid on the mapping quality according to the metrics of CE and T, (a) scenario I, (b) scenario II.

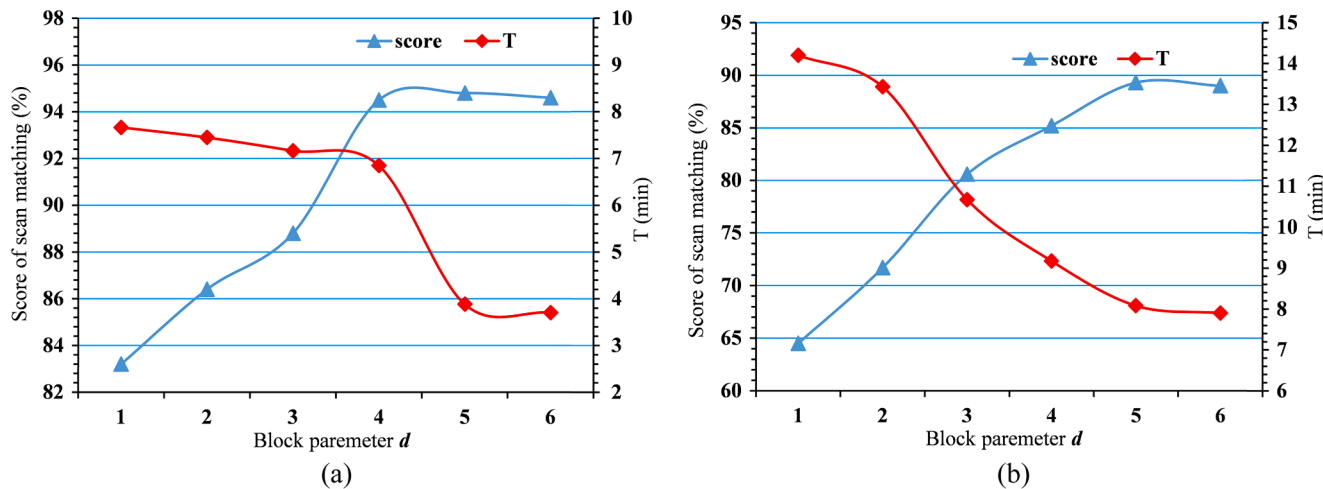


**Fig. 19.** Influence of the block parameter on the mapping quality according to the metrics of the mean score of scan matching and  $T$ , (a) scenario I, (b) scenario II.

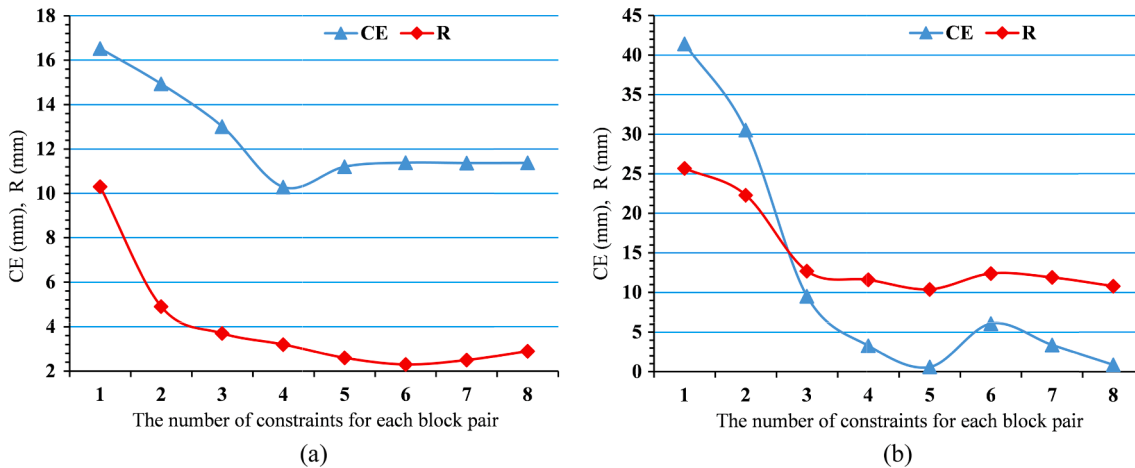


**Fig. 20.** The influence of the number of constraints on the mapping quality according to metrics of CE and  $R$ , (a) scenario I, (b) scenario II.

added to the constraints from the pose in the global pose optimization. Thus, cross-correction between the pose and map is achieved, improving the accuracy and robustness of LiDAR SLAM. The experimental results, using two different datasets for problematic scenarios, confirm that the proposed method can achieve high-accuracy 2D mapping. In comparison with 5 other advanced methods, our method is more robust against the problematic scenarios and generates more accurate maps. Moreover, the modeling results demonstrate that the proposed method can be applicable to efficient and accurate indoor modeling.

To the best of our review, there are many open datasets for the evaluation of LiDAR SLAM-based mapping methods. However, few open datasets can be used to evaluate the performance of the proposed method and other state-of-the-art methods because of the limited availability of the ground truth and the use of single types of sensors and different data formats. These factors make the evaluation challenging (Wang et al., 2018). The paper attempts to construct two standard datasets that contain the ground truths of the poses and maps and LiDAR and IMU data with common formats, but the ground-truth poses contain only dozens of high-precision checkpoints rather than all the poses. Therefore, future studies can improve upon our datasets and construct standard open datasets for the evaluation of LiDAR mapping. In addition, because dynamic objects will inevitably influence the mapping quality, we will take dynamic environments into account in future studies.

#### Declaration of Competing Interest

The authors declare that they have no known competing financial interests or personal relationships that could have appeared to influence the work reported in this paper.

#### Acknowledgment

This work was supported by the National Science and Technology Major Program (Grant Nos. 2018YFB1305003 and 2016YFB0502102) and the National Science Foundation of China (Grant Nos. 41771481 and 41671451).

#### References

- Bachrach, A., Prentice, S., He, R., Roy, N., 2011. RANGE-robust autonomous navigation in GPS-denied environments. *J. Field Robot.* 28 (5), 644–666.
- Baglietto, M., Sgorbissa, A., Verda, D., Zaccaria, R., 2011. Human navigation and mapping with a 6DOF IMU and a laser scanner. *Robot. Auton. Syst.* 59 (12), 1060–1069.
- Bailey, T., Durrant-Whyte, H., 2006. Simultaneous localization and mapping (SLAM): Part II. *IEEE Robot. Automat. Magaz.* 13 (3), 108–117.
- An, S.-Y., Kang, J.-G., Lee, L.-K., Oh, S.-Y., 2012. Line segment-based indoor mapping with salient line feature extraction. *Adv. Robot.* 26(5–6) 437–460.
- Becker, S., Peter, M., Fritsch, D., 2015. Grammar-supported 3d indoor reconstruction from point clouds for “As-Built” BIM, in: Pia15+Hrig15 - Joint Isprs Conference, Vol. II, vol. 2-3, U. Stilla and C. Heipke, Eds. (*ISPRS Annals of the Photogrammetry Remote Sensing and Spatial Information Sciences*, no. W4), 2015, pp. 17–24.

- Besl, P.J., McKay, N.D., 1992. A method for registration of 3-D shapes. *IEEE Trans. Pattern Anal. Mach. Intell.* 14 (2), 239–256.
- Biber, P., Ieee I., 2003. The normal distributions transform: A new approach to laser scan matching (Iros 2003: Proceedings of the 2003 Ieee/Rsj International Conference on Intelligent Robots and Systems, Vols 1-4). 2003, pp. 2743–2748.
- Blanco, J.L., Fernandez-Madrigal, J.A., Gonzalez, J., 2008. A Novel Measure of Uncertainty for Mobile Robot SLAM with Rao—Blackwellized particle filters. *Int. J. Robot. Res.* 27 (1), 73–89.
- Bosse, M., Zlot, R., 2008. Map matching and data association for large-scale two-dimensional laser scan-based SLAM. *Int. J. Robot. Res.* 27 (6), 667–691.
- G.A. Boyes, C. Ellul, D. Irwin, Exploring BIM for operational integrated asset management – a preliminary study utilising real-world infrastructure data. In: 12th 3D Geoinfo Conference 2017, 26–27 October 2017, Melbourne, Australia, 2017.
- Cadena, C., et al., 2016. Past, present, and future of simultaneous localization and mapping: toward the robust-perception age. *IEEE Trans. Robot.* 32 (6), 1309–1332.
- Carbone, L., Aragues, R., Castellanos, J.A., Bona, B., Jun 2014. A fast and accurate approximation for planar pose graph optimization. *Int. J. Robot. Res.* 33 (7), 965–987.
- Censi, A., Ieee, 2008. An ICP variant using a point-to-line metric. In: 2008 Ieee International Conference on Robotics and Automation, Vols 1–9(IEEE International Conference on Robotics and Automation ICRA, pp. 19–25.
- Choi, Y.-H., Lee, T.-K., Oh, S.-Y., 2008. A line feature based SLAM with low grade range sensors using geometric constraints and active exploration for mobile robot. *Autonom. Robot.* 24 (1), 13–27.
- Chong, Z.J., Qin, B., Bandyopadhyay, T., Ang, M.H., Jr., Fazzoli, E., Rus, D., 2013. Mapping with Synthetic 2D LiDAR in 3D Urban Environment. In: 2013 Ieee/Rsj International Conference on Intelligent Robots and Systems, N. Amato, Ed. (IEEE International Conference on Intelligent Robots and Systems, 2013, pp. 4715–4720.
- Cui, Li, Dong, 2019. Structural 3D reconstruction of indoor space for 5G signal simulation with mobile laser scanning point clouds. *Remote Sens.* 11 (19), 2262.
- D'Alfonso, L., Lucia, W., Muraca, P., Pugliese, P., 2015. Mobile robot localization via EKF and UKF: a comparison based on real data. *Robot. Auton Syst* 74, 122–127.
- Diaz-Vilarino L, Boguslawski P, Khoshelham K, Lorenzo H, Mahdjoubi L. Indoor navigation from point clouds: 3D modelling and obstacle detection. In: Xxiii Isprs Congress, Commission Iv, vol. 41, L. Halounova et al., Eds. (International Archives of the Photogrammetry Remote Sensing and Spatial Information Sciences, no. B4), 2016, pp. 275–281.
- Diosi, A., Kleeman, L., Ieee, Laser scan matching in polar coordinates with application to SLAM (2005 IEEE/RSJ International Conference on Intelligent Robots and Systems, Vols 1-4). 2005, pp. 1439–1444.
- Grisetti, G., Stachniss, C., Burgard, W., 2007. Improved techniques for grid mapping with Rao-Blackwellized particle filters. *IEEE Trans. Robot.* 23 (1), 34–46.
- Grisetti, G., Kuemmerle, R., Stachniss, C., Burgard, W., 2010. A tutorial on graph-based SLAM. *Iee Intell. Transport. Syst. Magaz.* 2 (4), 31–43.
- Gutmann, J.S., Weigel, T., Nebel, B., 2001. A fast, accurate and robust method for self-localization in polygonal environments using laser range finders. *Advanced Robotics* 14(8), 651–667.
- Hess, W., Kohler, D., Rapp, H., Andor, D., 2016. Real-time loop closure in 2D LiDAR SLAM. In: 2016 Ieee International Conference on Robotics and Automation, A. Okamura et al., Eds. (IEEE International Conference on Robotics and Automation ICRA, 2016, pp. 1271–1278.
- Himstedt, M., Frost, J., Hellbach, S., Boehme, H.-J., Maehle, E., Ieee, Large scale place recognition in 2D LiDAR scans using geometrical landmark relations, in: 2014 Ieee/Rsj International Conference on Intelligent Robots and Systems (IEEE International Conference on Intelligent Robots and Systems, 2014, pp. 5030–5035.
- Huang, S., Dissanayake, G., 2007. Convergence and consistency analysis for extended Kalman filter based SLAM. *IEEE Trans. Robot.* 23 (5), 1036–1049.
- Jensfelt, P., Kristensen, S., 2001. Active global localization for a mobile robot using multiple hypothesis tracking. *IEEE Trans. Robot. Automat.* 17 (5), 748–760.
- Kohlbrecher, S., Stryk, O.V., Meyer, J., Klingauf, U., 2011. A flexible and scalable slam system with full 3d motion estimation. In: 2011 IEEE International Symposium on Safety, Security, and Rescue Robotics, 2011.
- Konolige, K., Grisetti, G., Kuemmerle, R., Limketkai, B., Vincent, R., Ieee, 2010. Efficient sparse pose adjustment for 2D mapping. In: Ieee/Rsj 2010 International Conference on Intelligent Robots and Systems(IEEE International Conference on Intelligent Robots and Systems; 2010.
- Latif, Y., Cadena, C., Neira, J., 2013. Robust loop closing over time for pose graph SLAM. *Int. J. Robot. Res.* 32 (14), 1611–1626.
- Li, J., Zhan, H., Chen, B.M., Reid, I., Lee, G.H., 2017. Deep learning for 2D scan matching and loop closure. In: 2017 Ieee/Rsj International Conference on Intelligent Robots and Systems, A. Bicchi and A. Okamura, Eds. (IEEE International Conference on Intelligent Robots and Systems, 2017, pp. 763–768.
- S. L. A. B., G. L. A., L. W. A., and Y. Q. B., SLAM integrated mobile mapping system in complex urban environments. *ISPRS J. Photogram. Remote Sens.*, 166, 316–332.
- Lu, F., Milios, E., 1997. Robot pose estimation in unknown environments by matching 2D range scans. *J. Intell. Robot. Syst.* 18 (3), 249–275.
- Ochmann, S., Vock, R., Wessel, R., Klein, R., 2016. Automatic reconstruction of parametric building models from indoor point clouds. *Comput. Graph.-UK* 54, 94–103.
- Ochmann, S., Vock, R., Klein, R., 2019. Automatic reconstruction of fully volumetric 3D building models from point clouds. *ISPRS J. Photogram. Remote Sens.* 151, 251–262.
- Oesau, S., Lafarge, F., Alliez, P., 2014. Indoor scene reconstruction using feature sensitive primitive extraction and graph-cut. *ISPRS J. Photogram. Remote Sens.* 90, 68–82.
- Olson, E.B., Ieee, Real-time correlative scan matching. In: Icra: 2009 Ieee International Conference on Robotics and Automation, Vols 1-7(IEEE International Conference on Robotics and Automation ICRA, 2009), pp. 1233–1239.
- Olson, E., Ieee, 2015. M3RSM: many-to-many multi-resolution scan matching. In: 2015 Ieee International Conference on Robotics and Automation(IEEE International Conference on Robotics and Automation ICRA, pp. 5815–5821.
- Opromolla, R., Fasano, G., Grassi, M., Savvaris, A., Moccia, A., 2017. PCA-based line detection from range data for mapping and localization-aiding of UAVs. *Int. J. Aerospac Eng.*
- Qian, C., Zhang, H., Tang, J., Li, B., Liu, H., 2019. An orthogonal weighted occupancy likelihood map with IMU-aided laser scan matching for 2D indoor mapping. *Sensors* 19(7), 2019, Art. no. 1742.
- Quan, M., Piao, S., Tan, M., Huang, S.-S., 2019. Accurate monocular visual-inertial SLAM using a map-assisted EKF approach. *Ieee Access*, 7, pp. 34289–34300.
- Rafiee, A., Dias, E., Fruittier, S., Scholten, H., Tel, 2014. From BIM to geo-analysis: view coverage and shadow analysis by BIM/GIS integration. *International Conference on Design & Decision Support Systems in Architecture & Urban Planning*.
- Ren, R., Fu, H., Wu, M., 2019. Large-scale outdoor SLAM based on 2D Lidar. *Electronics* 8 (6), Art. no. 613.
- Tang, J., Chen, Y., Jaakkola, A., Liu, J., Hyypa, J., Hyypa, H., 2014. NAVIS-An UGV indoor positioning system using laser scan matching for large-area real-time applications. *Sensors* 14 (7), 11805–11824.
- Thrun, S., 2001. An online mapping algorithm for teams of mobile robots. *Int. J. Robot. Res.* 20 (20), 335–363.
- Thrun, S., Burgard, W., Fox, D., 1998. A probabilistic approach to concurrent mapping and localization for mobile robots. *Auton. Robot.* 5(3-4), 253–271.
- S. Thrun, W. Burgard, and D. Fox, “A Real-Time Algorithm for Robot Mapping with Applications to Multirobot and 3D Mapping,” in IEEE Int. Conf. on Robotics and Automation, 2000.
- Wang, C., et al., 2018. Semantic line framework-based indoor building modeling using backpacked laser scanning point cloud. *ISPRS J. Photogram. Remote Sens.* 143, 150–166.
- Wang, Z., Chen, Y., Mei, Y., Yang, K., Cai, B., 2018. IMU-assisted 2D SLAM method for low-texture and dynamic environments. *Appl. Sci.-Basel* 8(12), Art. no. 2534.
- Wen, J., Qian, C., Tang, J., Liu, H., Ye, W., Fan, X., 2018. 2D LiDAR SLAM back-end optimization with control network constraint for mobile mapping. *Sensors* 18(11), Art. no. 3668.
- Wu, H., Xu, Z., Wu, G., 2019. A novel method of missing road generation in city blocks based on big mobile navigation trajectory data. *ISPRS Int J Geo-Inform* 8(3), 2019, Art. no. 142.
- Yatim, N.M., Buniyamin, N., 2015. Particle filter in simultaneous localization and mapping (slam) using differential drive mobile robot,“ *Jurnal Teknologi* 77(20), 91–97.
- Zhang, T., Wu, K., Song, J., Huang, S., Dissanayake, G., 2017. Convergence and consistency analysis for a 3-D invariant-EKF SLAM. *IEEE Robot. Automat. Lett.* 2 (2), 733–740.